Cell Reports

Article

Identification of the core regulatory program driving NEUROD1-induced neuronal reprogramming

Graphical abstract

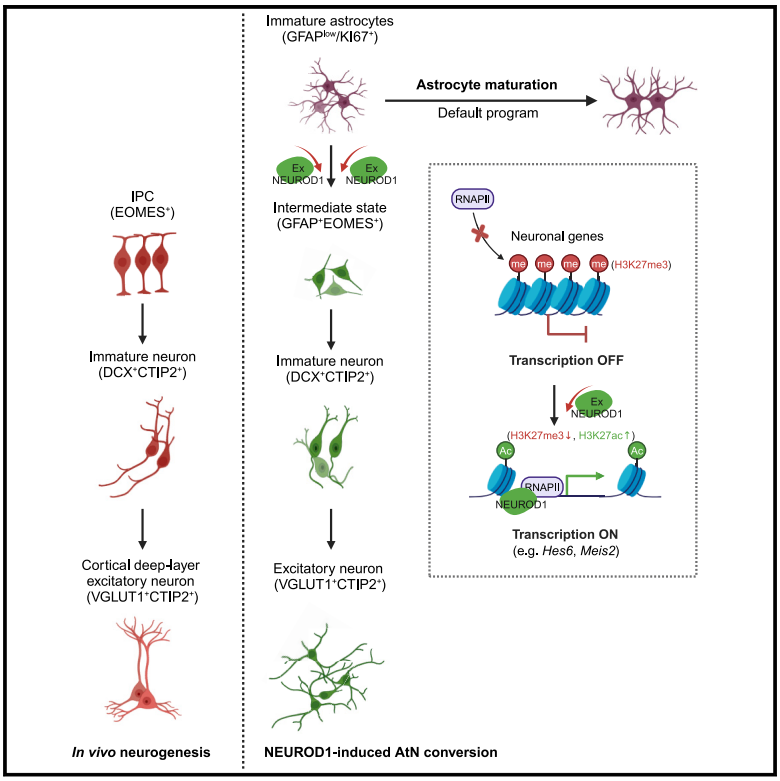

Highlights

- ND1-induced ImA-to-neuron conversion transiently activates astrocyte and neuronal genes
- The trajectory of ND1-induced neuronal reprogramming mimics that of *in vivo* neurogenesis
- NEUROD1 swiftly alters the open chromatin landscape of ImAs by inducing H3K27ac
- 25 NEUROD1 targets were identified as key regulators, including *Hes6*

Authors

Wen Li, Dan Su, Xining Li, ..., Xiaopeng Luo, Gong Chen, Xiaoying Fan

Correspondence

gongchen@jnu.edu.cn (G.C.), fan_xiaoying@gzlab.ac.cn (X.F.)

In brief

Li et al. utilized single-cell and bulk multiomics sequencing techniques to capture the trajectory of *in vitro* ND1-induced neuronal reprogramming and uncover critical regulations at both transcriptomic and chromatin levels.

Li et al., 2025, Cell Reports *44*, 115523
April 22, 2025
https://doi.org/10.1016/j.celrep.2025.115523

CellPress

Cell Reports

CellPress
OPEN ACCESS

Article

Identification of the core regulatory program driving NEUROD1-induced neuronal reprogramming

Wen Li,[2,4,6] Dan Su,[1,3,6] Xining Li,[1,3,6] Kang Lu,[2,6] Qingpei Huang,[1,3] Jiajun Zheng,[2,5] Xiaopeng Luo,[2] Gong Chen,[2,4,*] and Xiaoying Fan[1,3,7,*]

[1]GMU-GIBH Joint School of Life Sciences, The Fifth Affiliated Hospital of Guangzhou Medical University, Guangzhou National Laboratory, Guangzhou Medical University, Guangzhou 510005, China
[2]Guangdong-HongKong-Macau Institute of CNS Regeneration (GHMICR), Jinan University, Guangzhou 510632, China
[3]The Bioland Laboratory, Guangzhou 510700, China
[4]Key Laboratory of CNS Regeneration (Ministry of Education), Guangdong Key Laboratory of Non-Human Primate Research, GHM Institute of CNS Regeneration, Jinan University, Guangzhou 510632, China
[5]Department of Anesthesiology, Guangzhou First People's Hospital, Guangzhou 510180, China
[6]These authors contributed equally
[7]Lead contact
*Correspondence: gongchen@jnu.edu.cn (G.C.), fan_xiaoying@gzlab.ac.cn (X.F.)
https://doi.org/10.1016/j.celrep.2025.115523

SUMMARY

NEUROD1 (ND1)-induced astrocyte-to-neuron (AtN) conversion shows promise for treating neurological disorders. To gain insight into the molecular mechanisms of neuronal reprogramming, we established an *in vitro* system using primary cortical astrocyte cultures from postnatal rats and employed single-cell and multiomics sequencing. Our findings indicate that the initial cultures primarily consisted of immature astrocytes (ImAs), with potentially a minor presence of radial glial cells. The ImAs initially went through an intermediate state, activating both astrocyte and neural progenitor genes. Subsequently, they mimic *in vivo* neurogenesis to acquire mature neuronal characteristics. We show that ND1 acted as a pioneer factor that reshapes the chromatin landscape of astrocytes to that of neurons. This restructuring promotes the expression of neurogenic genes via inducing H3K27ac modification. Through integrative analysis of various ND1-induced neuronal specification systems, we identified 25 ND1 targets, including *Hes6*, as key regulators. Thus, our work highlights the key role of ND1 and its downstream regulators in neuronal reprogramming.

INTRODUCTION

Adult mammalian neurogenesis is limited in terms of the number and region of occurrence.[1,2] Therefore, strategies that promote endogenous neurogenesis hold great potential for therapeutic interventions for neurological disorders.[2–4] Unlike neurons, macroglial cells, including astrocytes and oligodendrocyte progenitors (OPCs), can reactivate and proliferate under conditions of injury and disease.[5] These reactive glia exhibit characteristics similar to neural stem cells (NSCs) and can give rise to a few immature neurons under specific circumstances.[6–9] The latent neurogenic capacity of these cells can be enhanced through ectopic expression of pro-neuronal transcription factors (TFs), microRNA interference, PTBP1 knockdown (KD), or small-molecule treatment, both *in vitro* and *in vivo*.[2,3] *In vivo* neuronal reprogramming from glial cells has shown therapeutic effects in animal models of various neurological diseases.[9–13]

NEUROD1 (ND1) is an important TF involved in embryonic and postnatal neuronal development.[14,15] It has been shown to rapidly and efficiently convert astrocytes into functional neurons, both *in vitro* and *in vivo*.[16] A previous study examined the gene expression regulations of ND1-mediated astrocyte-to-neuron (AtN) conversion through bulk RNA sequencing (RNA-seq),[17] providing information on gene expression changes at different time points. The reprogramming process is very complicated, involving different cellular statuses and orchestrated molecular programs, which are largely masked in bulk sequencing. Thus, we still lack a full understanding of the dynamic process and molecular regulations underlying the conversion of astrocytes to neurons by ND1.

To illuminate the underlying mechanism of ND-induced AtN conversion, we have established an *in vitro* platform of ND1-induced neuronal reprogramming, which enables tracing the conversion of starting astrocytes to neurons without contamination of endogenous neurons. Then, single-cell and bulk multiomics sequencing was used to elucidate how astrocytes isolated from the postnatal rat cortex are converted into neurons and unravel the underlying molecular regulations, including gene expression, chromatin accessibility, and multiple histone modifications.

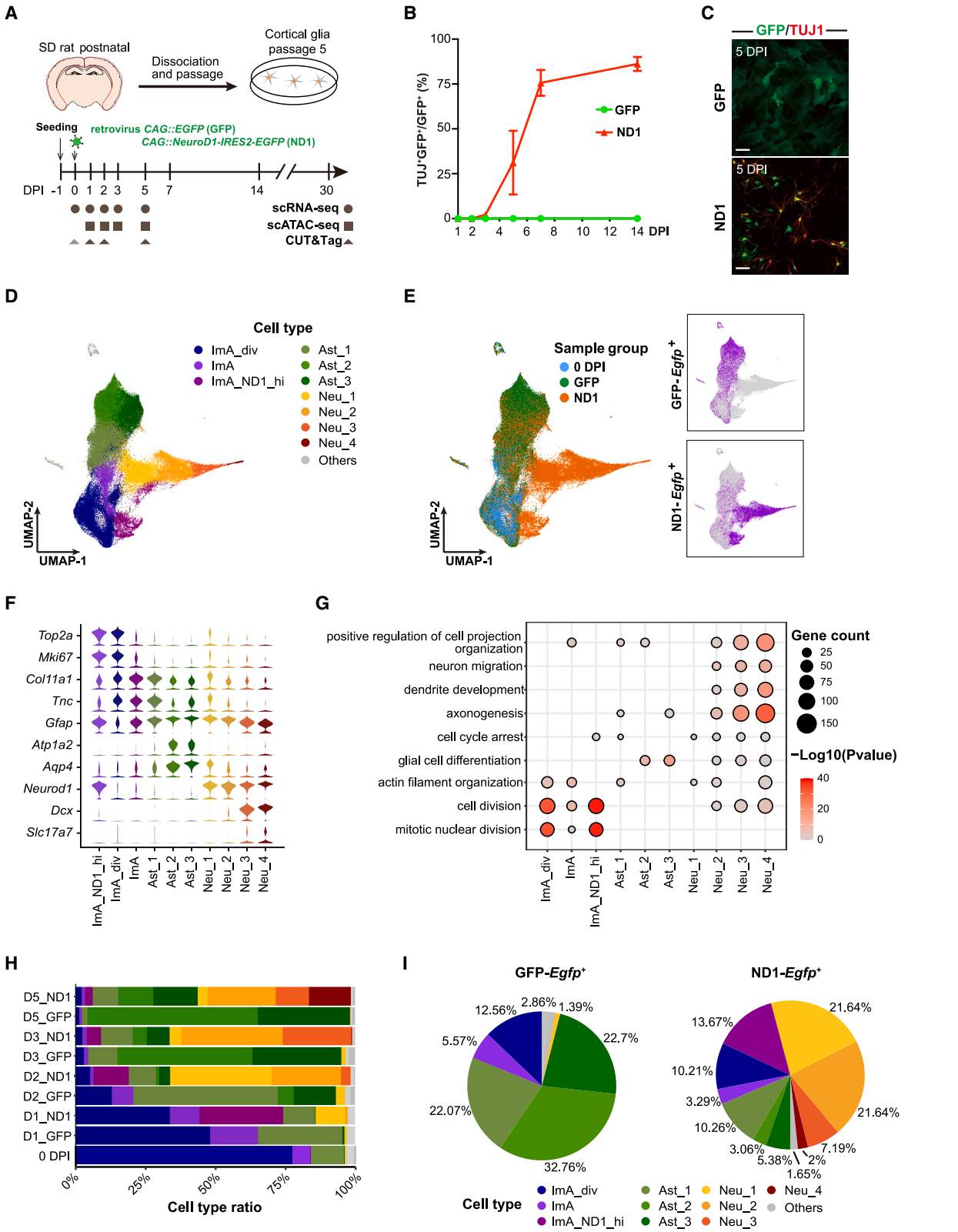

(legend on next page)

RESULTS

scRNA-seq captures diverse intermediate cell states during ND1-induced neuronal reprogramming

To investigate the cellular mechanisms underlying ND1-induced AtN reprogramming, we established an *in vitro* transdifferentiation platform. Primary astrocytes were isolated from cerebral cortices of postnatal rats and subcultured for 5 passages in the presence of 10% serum to reduce progenitor cells before being transduced with a retrovirus carrying the *CAG::NeuroD1-IRES-EGFP* (ND1) construct (Figures 1A and S1A–S1C). The retrovirus carrying the *CAG::EGFP* (GFP) construct acted as a control. The expression of ND1 was detectable as early as 1 day post-infection (DPI; Figure S1E). Following ND1 expression, the astrocytes gradually changed their morphology and started expressing TUJ1, a classical neuronal marker, beginning 3 DPI (Figure S1F). The proportion of $TUJ1^+$ cells increased over time (Figures 1B and S1F). By 14 DPI, approximately 80% of GFP^+ cells had become $TUJ1^+$. In contrast, the control group showed negligible TUJ1 expression at all time points examined (Figures 1B and S1C–S1E). In addition to TUJ1, other immature and mature neuron markers, including DCX, NEUN, MAP2, and SV2, were also observed following ND1 transduction (Figures S1G–S1J). Over 90% of the converted neurons were excitatory neurons expressing VGLUT1, with high ratios of $TBR1^+$ and $CTIP2^+$ cells (Figures S1H and S1J). Furthermore, the 30 DPI neurons acquired electrophysiological features similar to those isolated from embryonic day (E)16.5 rat cortices (Figures S2A–S2H). They predominantly formed functional excitatory neuronal circuits, exhibiting frequencies and amplitudes comparable to those primary neurons (Figures S2I–S2L). These results demonstrate a rapid and efficient *in vitro* ND1-induced neuronal reprogramming platform using rat astrocytes, similar to previous studies conducted with mouse or human primary astrocytes.[16]

Then, we investigated the reprogramming mechanism through single-cell multiomics analyses (Figure 1A). Firstly, we generated a single-cell RNA-seq (scRNA-seq) dataset composed of cells from 0 to 5 DPI, when apparent fate conversion to neurons occurs (Figure 1C), to capture the continuous cellular states during the reprogramming process. After quality control, we retained 13,081 cells from 0 DPI, 32,741 cells from the GFP control group, and 46,164 cells from the ND1 group for further clustering (Figures 1D and 1E). Based on a panel of known markers, we identified three major cell types: immature astrocyte (ImA), astrocyte, and neuron (Figures 1D, 1F, and Table S1A). The ImA population could be further divided into three subclusters: ImA_div, ImA, and ImA_ND1_hi. They all exhibited high expression of *Gfap* and *Tnc* (Figure 1F). ImA_div cells showed high activity in the cell cycle, while ImA_ND1_hi shared many features with ImA_div but expressed high levels of *Neurod1* (Figure 1F). The astrocyte cluster consisted of three subclusters, including Ast_1, which expressed high levels of *Gfap*, *Tnc*, and *Col11a1*, and Ast_2 and Ast_3, which expressed high levels of *Atp1a2* and *Aqp4* (Figure 1F). The neuronal cluster comprised four subclusters (Neu_1 to Neu_4) that featured high expression of neuronal markers and genes enriched in Gene Ontology (GO) terms related to axonogenesis, dendrite development, neuron migration, and positive regulation of cell projection (Figures 1F and 1G).

Notably, the start cells (0 DPI; Figure S1) were predominantly identified as ImAs (approximately 80%; Figure 1H). The GFP control cells were primarily classified as ImAs and astrocytes (Figures 1E, 1H, and 1I), while the majority of cells in the ND1 group were categorized into neuronal subclusters (Figure 1E). Among the $Egfp^+$ cells in the ND1 group, 52.5% belonged to the neuronal clusters, 13.7% were ImA_ND1_hi cells, and 32.2% were ImAs and astrocytes (Figure 1I). These findings represent continuous cell states during the cell fate switch from ImAs to neurons induced by ND1.

An intermediate state expressing both astrocytic and neuron progenitor genes in ND1-induced neuronal reprogramming

We then conducted pseudotime analysis to uncover the relationships between different cell subclusters during cell fate specification. There were two distinct developmental branches originating from the ImAs (Figures 2A and S3A). As indicated by the expression patterns of the astrocyte marker *Aqp4* and the neuron marker *Tubb3*, we defined these two branches as the astrocyte branch and neuron branch, respectively (Figures 2B and S3A). Importantly, the real sampling time points aligned well with the pseudotemporal axis, underscoring a remarkable consistency between the actual and inferred developmental trajectories (Figures 2A and 2C).

To gain further insights into the molecular programs driving the conversion process, we extracted pseudotime genes along both trajectory branches and performed clustering analysis

Figure 1. Cell type diversity in ND1-induced AtN conversion

(A) Schematic of setting up the *in vitro* AtN conversion system and sequencing strategies at indicated time points. The light triangle indicates the absence of ND1 CUT&Tag at 0 DPI.

(B) Quantitation revealing the increase in the ratio of converted neurons indicated by immunostaining of TUJ1 in GFP^+ cells in the ND1 group along the infection time. See also Figure S1F. TUJ1 rates in the GFP group: 1 DPI = 0.0% ± 0.0%; 2 DPI = 0.02% ± 0.02%; 3 DPI = 0.03% ± 0.03%; 5 DPI = 0.0% ± 0.0%; 7 DPI = 0.0% ± 0.0%; and 14 DPI = 0.0% ± 0.0%. TUJ1 rates in the ND1 group: 1 DPI = 0.02% ± 0.02%; 2 DPI = 0.02% ± 0.01%; 3 DPI = 2.2% ± 1.0%; 5 DPI = 31.2% ± 10.3%; 7 DPI = 75.6% ± 4.2%; and 14 DPI = 86.2% ± 2.2%.

(C) Representative imaging showing $TUJ1^+$ (red) neurons at 5 DPI. Scale bar: 50 μm.

(D) Uniform manifold approximation and projection (UMAP) showing the cell types identified in the *in vitro* ND1-induced AtN system.

(E) Group information of each cell on the UMAP. The $Egfp^+$ cells in each group are shown on the right.

(F) Violin plots showing the expression levels of classical markers in each cell type.

(G) Representative GO terms of the DEGs for each cell type.

(H) The ratios of all cell types in each sample collected at indicated time points. Cell types are colored the same as in (D).

(I) The ratios of all cell types within the $Egfp^+$ cells in the ND1 and GFP groups, respectively.

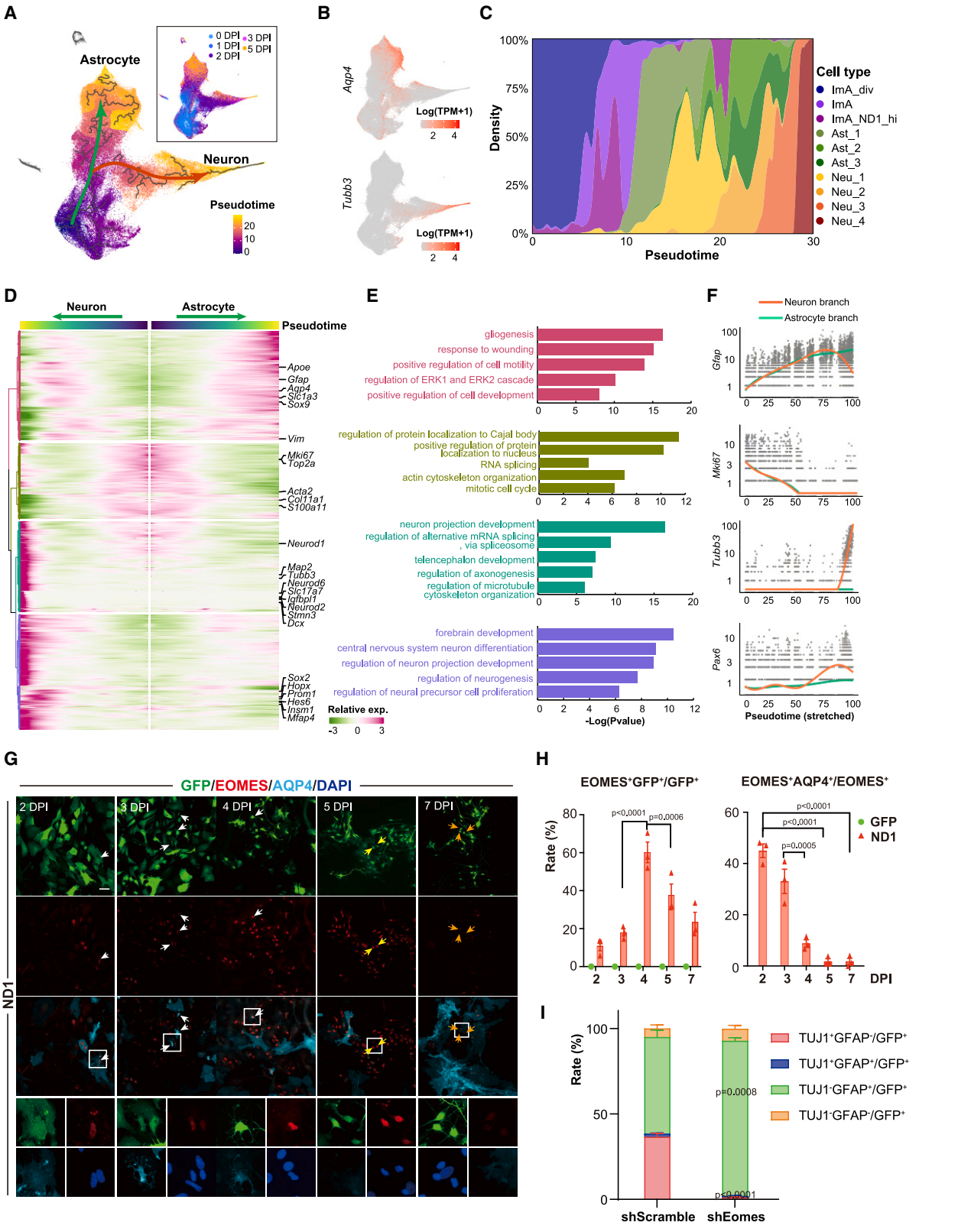

(legend on next page)

(Figure 2D). In the astrocyte branch, the ImAs initially downregulated cell-cycle-related genes (Figure 2E; e.g., *Mik67* and *Top2a*) and subsequently upregulated genes involved in glial differentiation, including gliogenesis-related genes like *Gfap*, *Aqp4*, and *Apoe* (Figures 2D–2F and S3D). On the other hand, the ImAs transduced with ND1 in the neuron branch also initially downregulated cell cycle genes but then underwent an intermediate state, simultaneously upregulating genes associated with glial differentiation and early neurogenesis genes like *Pax6* and *Sox2* (Figures 2D–2F and S3D). As the conversion proceeds, the intermediate cells gradually decreased genes related to gliogenesis and concomitantly increased genes associated with neuronal development events, including neuron projection development and regulation of neurogenesis, e.g., *Tubb3* and *Dcx* (Figures 2D–2F and 1B).

Previous studies have suggested that ND1-induced AtN conversion bypasses the NSC stage,[16] so we examined the expression levels of neural progenitor markers including *Sox2*, *Pax6*, *Eomes* (*Tbr2*), and *Dcx*.[14] Interestingly, *Sox2* and *Pax6* were transiently upregulated slightly in the early stage but quickly downregulated (Figures 2F and S3B). Subsequently, *Eomes* and *Dcx* increased constantly (Figure S3B). The immunostaining result supported the transient increase in the number of $EOMES^+$ cells (Figures 2G and 2H) in the GFP^+ population of the ND1 group, and the $EOMES^+AQP4^+$ cells accounted for 50% of $EOMES^+$ cells, whose proportion reduced as the conversion proceeded (Figures 2G and 2H). To validate whether the intermediate progenitor cell (IPC) stage is necessary for successful reprogramming, we knocked down *Eomes* through short hairpin RNA (shRNA) (Figure S3E). Interestingly, knocking down *Eomes* abolished the ND1-mediated AtN conversion (Figure 2I). These data suggest the presence of a transient intermediate stage co-expressing astrocytic genes and neuronal progenitor genes during the neuronal reprogramming of ImAs.

To further elucidate the gene regulatory networks, we performed weighted correlation network analysis (WGCNA) and identified six gene modules closely associated with different cell types and states (Figures S3F–S3I and Table S2). The yellow module contained genes involved in cell division and exhibited a high score in the initial ImAs. The red module was shared by cells in the early stages of both lineages, enriched in genes participating in immune response (interleukin [IL]-7 response) and metabolism (ATP metabolic process and cell redox homeostasis). In contrast, the brown module was enriched in late-stage cells of both lineages, comprising genes involved in metabolic processes (response to nitrogen starvation and hormone metabolic process). The shift from the red module to the brown module along the pseudotemporal axis suggests a metabolic change during fate commitment and maturation (Figure S3G). The astrocyte-associated network consists of two modules: the green module active along the astrocyte lineage and the turquoise module restricted to the late stage of astrocyte differentiation. Specifically, the green module was enriched in genes involved in glial cell proliferation and response to the transforming growth factor β (TGF-β) pathway, while the turquoise module contained genes that promote astrocyte differentiation and suppress the neurogenesis process. The blue module comprised genes regulating neural progenitor proliferation and telencephalon development. These modules derived from WGCNA showed high consistency with the previously identified gene clusters from pseudotime analysis, further supporting the regulatory networks in ND1-induced AtN reprogramming.

ND1-induced neuronal reprogramming partly resembles cortical deep-layer neurogenesis

In the developing cortex, ND1 has been identified as a critical TF involved in the specification of deep-layer neurons.[14] In this study, the majority of ND1-reprogrammed neurons were identified as cortical excitatory neurons (Figures S1H and S1K). We wondered whether the reprogramming and cortical development share similar cellular compartments and molecular regulations.

To address this question, we first profiled cells from E16.5 and postnatal day (P)2 rat cerebral cortices using scRNA-seq (Figures 3A, S4A, and Table S1B). We found that deep-layer neurons were predominantly captured from E16.5, while upper-layer neurons were mainly detected at P2. The cell composition was further confirmed by immunostaining (Figures S4C and S4D). We then compared the cell identity between the two systems. As expected, the ImA and astrocyte subclusters were assigned to astrocytes *in vivo* (Figures 3B and S4E). The Neu_1 cells were primarily aligned with astrocytes *in vivo*, and the

Figure 2. Trajectories of ImA to neuron reprogramming and astrocyte development

(A) Pseudotime score of the cells on UMAP. Two branches are figured out. The real sampling time for the cells are shown in the box.

(B) The expression of astrocyte marker *Aqp4* and neuron maker *Tubb3*.

(C) Density distribution of each cell type along the pseudotime.

(D) Heatmap showing the expression patterns of the pseudotime genes along the two branches.

(E) GO terms of genes corresponding to the groups in (D).

(F) Relative expression of representative genes corresponding to the four groups in (D).

(G) Time-lapse images showing that intermediate cells co-express EOMES and AQP4 (white arrows) during neuronal reprogramming. The yellow arrows indicate $EOMES^+AQP4^-$ cells. Scale bar: 50 μm. See also Figures S3C.

(H) Histograms showing quantitation of (G). $EOMES^+GFP^+$ rates in the GFP group: 2 DPI = 0.0% ± 0.0%; 3 DPI = 0.0% ± 0.0%; 4 DPI = 0.0% ± 0.0%; 5 DPI = 0.0% ± 0.0%; and 7 DPI = 0.0% ± 0.0%. $EOMES^+GFP^+$ rates in the ND1 group: 2 DPI = 10.9% ± 2.6%; 3 DPI = 18.0% ± 1.9%; 4 DPI = 60.2% ± 5.4%; 5 DPI = 37.5% ± 6.0%; and 7 DPI = 23.5% ± 5.1%. Two-way ANOVA followed by Sidak's multiple comparisons test. $EOMES^+AQP4^+$ rates in the ND1 group: 2 DPI = 45.0% ± 2.7%; 3 DPI = 33.0% ± 4.8%; 4 DPI = 8.8% ± 1.4%; 5 DPI = 1.9% ± 1.0%; and 7 DPI = 1.8% ± 1.2%. One-way ANOVA followed by Tukey's multiple comparisons test.

(I) Histogram showing that *Eomes* KD abolished ND1-induced AtN conversion. shScramble: $TUJ1^+GFAP^-/GFP^+$ = 36.5% ± 2.1%; $TUJ1^+GFAP^+/GFP^+$ = 1.9% ± 0.3%; $TUJ1^-GFAP^+/GFP^+$ = 56.4% ± 4.1%; and $TUJ1^-GFAP^-/GFP^+$ = 5.1% ± 2.1%. shEomes: $TUJ1^+GFAP^-/GFP^+$ = 1.0% ± 0.4%; $TUJ1^+GFAP^+/GFP^+$ = 1.0% ± 0.2%; $TUJ1^-GFAP^+/GFP^+$ = 90.8% ± 1.8%; and $TUJ1^-GFAP^-/GFP^+$ = 7.0% ± 2.1%. Unpaired t test.

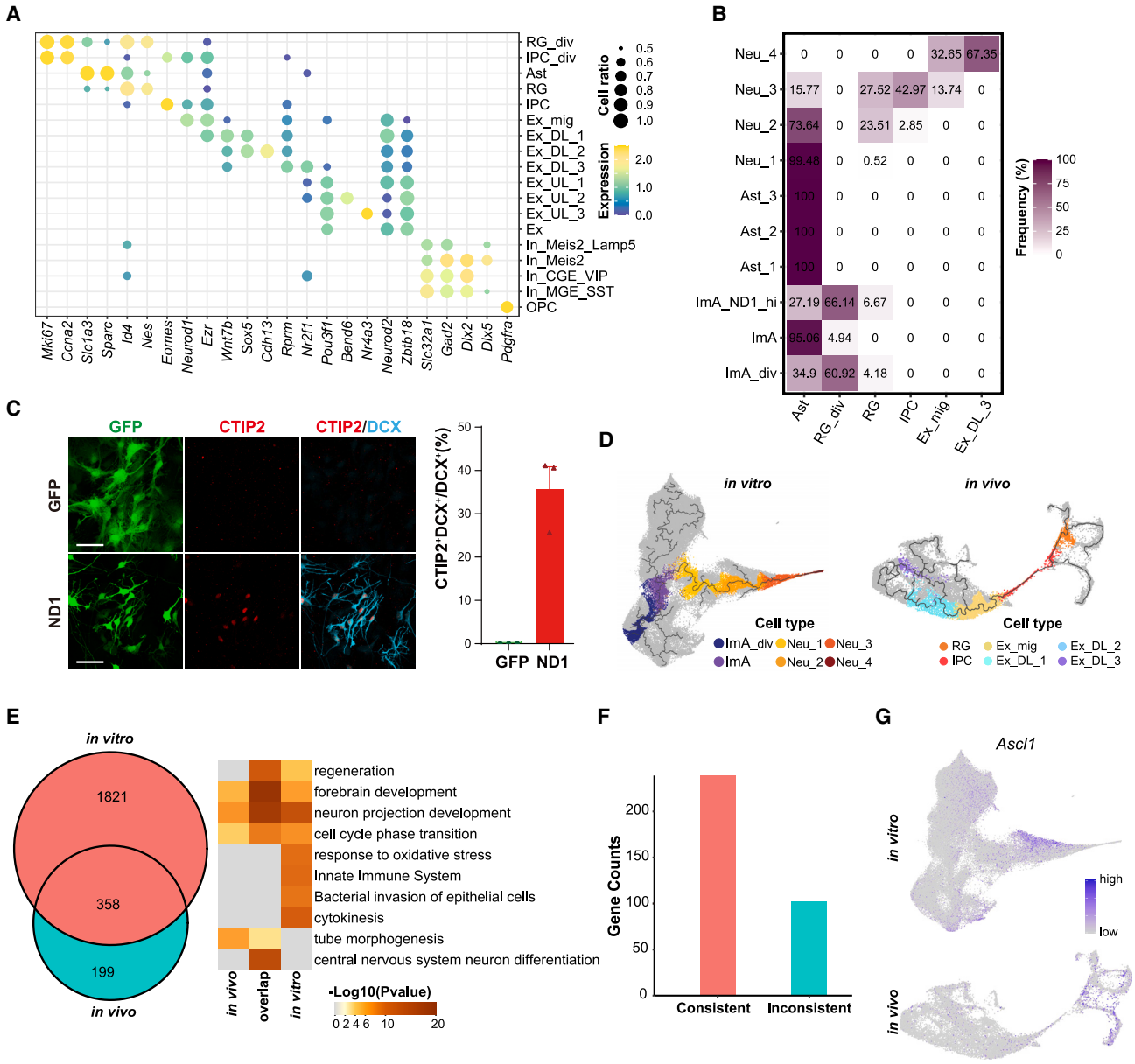

Figure 3. Comparison of ND1-induced neuronal reprogramming to the *in vivo* neurogenesis

(A) Dot plots showing the expression levels of the markers in each cell type identified in the *in vivo* cortices. See also Figure S4A.

(B) The congruent relationship of *in vitro* and *in vivo* cell types.

(C) Representative images and quantitation showing the appearance of the deep-layer marker CTIP2 (red) in converted neurons (GFP^+DCX^+) at 5 DPI in the ND1 group, $CTP2^+DCX^+/DCX^+ = 35.8\% \pm 5.1\%$. Scale bar: 50 μm.

(D) The neuronal trajectories captured *in vitro* and *in vivo*. Relevant cell types are shown.

(E) Venn diagram showing comparison of genes between *in vitro* and *in vivo* trajectories. GO terms of the three group of genes are shown on the right.

(F) Consistency of expression patterns of the 358 genes between *in vivo* and *in vitro* trajectories.

(G) The expression level of endogenous *Ascl1* in *in vivo* and *in vitro* cells.

subsequent neuronal subclusters exhibited a gradual transition from astrocytes to Ex_DL_3 through the radial glial cell (RG cell; also regarded as NSCs) and IPC states (Figures 3B and S4E). Immunostaining of the ND1-transduced cells proved the presence of $CTIP2^+$ neurons as early as 5 DPI (Figure 3C). These findings suggest that ND1 might induce a transdifferentiation program that mimics the neurogenic paradigms of neurogenesis, progressing from RGs to IPCs and finally to deep-layer excitatory neurons (Figures 2G and 2H).

We then investigated whether the WGCNA modules identified *in vitro* were involved in neurogenesis (Figures S3E–S3H and S4F). The turquoise module associated with astrocyte

CellPress
OPEN ACCESS

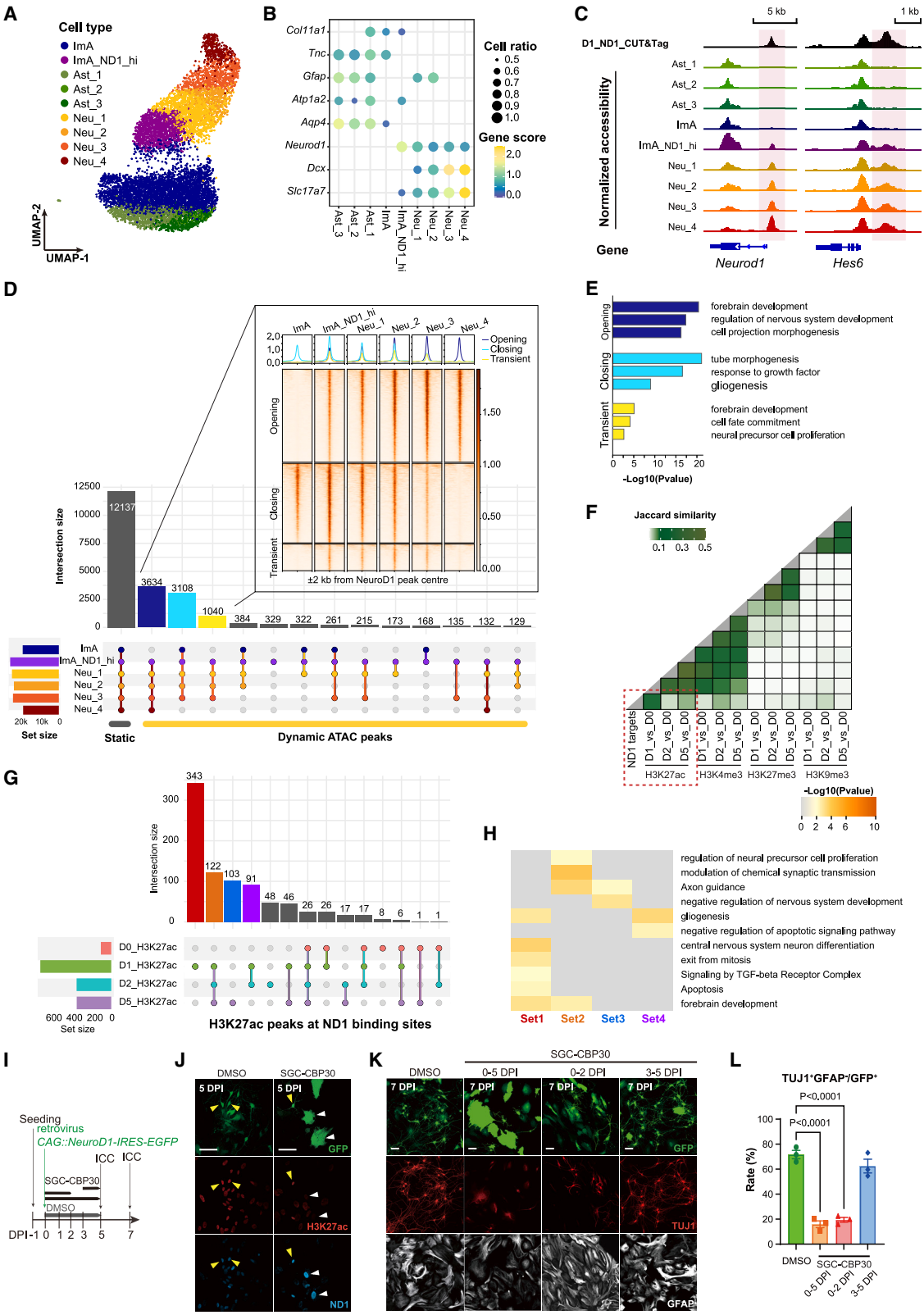

(legend on next page)

differentiation was highly active in astrocytes *in vivo*, while the blue module relating to neurogenesis was highly active in IPCs and migrating neurons. The yellow module associated with ImAs was highly active in dividing RG cells and IPCs. To examine this in more detail, we performed pseudotime analysis of the *in vivo* cells and identified a trajectory originating from RG cells (Figures S4G and S4H). When comparing the trajectory genes extracted from the *in vitro* and *in vivo* datasets (Figure 3D and Table S3), we obtained 358 shared genes, accounting for 64% of the pseudotime genes observed *in vivo* (Figure 3E). The shared genes were mainly categorized into biological pathways related to neuronal development and differentiation (Figure 3E). 67% of these genes exhibited the same expression pattern along the pseudotime trajectories (Figures 3F and S4I). Meanwhile, the reprogramming also exhibited unique regulatory modes. For example, there were 1,821 specific genes involved in the response to innate immune and oxidative stress (Figure 3E), suggesting that those genes were likely induced by viral infection and promoted cell fate switch from astrocytes to neurons. Notably, *Ascl1*, which was hardly expressed in cortical excitatory neurogenesis, was transiently upregulated in the early intermediate cells during AtN conversion (Figure 3G). The temporal increase of *Ascl1* has also been reported in the conversion of glial cells to neuroblasts *in vivo*, suggesting some common regulatory pathways during AtN conversion.[18–20]

ND1 reshapes the chromatin landscape and promotes neuronal genes expression by inducing H3K27ac

To gain insight into chromatin remodeling during ND1-driven neuronal reprogramming, we performed scATAC-seq (single-cell assay for transposase-accessible chromatin with high-throughput sequencing) on cells from the ND1 group (Figure 1A). All cell types identified in the scRNA-seq data were classified except for ImA_div cells, as the cell cycle characteristics are masked in scATAC-seq data[21] (Figure 4A). The gene scores of cell type markers validated the cell type annotation. Importantly, Neu_1 and Neu_2 clusters displayed high scores of both the astrocytic gene *Gfap* and the immature neuronal gene *Dcx*, supporting the transitional stage of converting cells in between astrocytes and neurons during the conversion process (Figure 4B). Genome browser visualization also proved that ATAC peaks in the astrocytic genes, including *Aqp4* and *Gfap*, were observed in all cell subclusters except the late neuronal subcluster Neu_4 (Figure S5A). Concomitantly, the ATAC peaks in the neural progenitor genes (*Eomes*) were induced immediately into the ImA_ND1_hi and maintained high accessibility in the subsequent neuronal clusters (Figure S5A). These results indicate that exogenous ND1 rapidly reshapes the chromatin accessibility landscape of astrocytes to favor neuronal reprogramming.

To illuminate how ND1 changed the chromatin accessibility landscape of the ImAs, we performed CUT&Tag (cleavage under targets and release using Tn5 tagmentation; hereafter termed CNT) sequencing to temporally assay the binding of ND1 to chromatin and investigated the histone modifications, including H3K4me3, H3K27ac, H3K27me3, and H3K9me3, of the ND1-occupied loci (Figure 1A). Overall, the CNT peaks of ND1, H3K27me3, and H3K9me3 were enriched in intergenic regions (Figure S5B). H3K27ac CNT peaks were enriched in both intergenic regions and promoters, while the H3K4me3 CNT peaks were highly enriched in promoters (Figure S5B). Within 24 h after the transduction, exogenous ND1 directly bound the endogenous promoter and enhancer of *Neurod1* and *Hes6* and increased the accessibility of these loci (Figure 4C). This is consistent with the previous study reporting ND1 as a self-regulator.[22] When analyzing the chromatin accessibility of the ND1-occupied loci of all time points, we found that approximately 45% of them dynamically changed across the conversion process (Figure 4D). The top three categories of dynamic peaks were ND1-opening loci whose chromatin was continuously open after ND1 overexpression, ND1-closing loci that were gradually closed, and ND1-transient loci that were transiently opened in the intermediate cells but closed in the final converted neurons (Figure 4D and Table S4). The ND1-opening loci were the most abundant, and the corresponding genes were enriched in forebrain development, regulation of nervous system development, and cell projection morphogenesis. ND1-closing loci included genes associated with tube morphogenesis, response to growth factors, and gliogenesis. ND1-transient loci were related to cell fate commitment and neural precursor cell proliferation (Figure 4E). These results provide evidence at the epigenetic level that ND1 reprogrammed astrocytes to neurons through a transient progenitor state and gradually silenced the astrocyte genes at a later stage.

Figure 4. Dynamic chromatin remodeling and histone modification induced by ND1

(A) UMAP showing the cell types identified from scATAC-seq.

(B) Dot plots showing gene scores of the classical markers in each cell type.

(C) ND1 CNT at day 1 and pseudobulk ATAC tracks at *Neurod1* and *Hes6* gene loci. The pink frame indicates ND1-binding sites with increasing chromatin accessibility.

(D) UpSet plot showing the ATAC peaks of ImA and neuronal clusters at the top 10% ND1-binding sites. The top 3 dynamic ATAC sets highlighted with different colors are defined as opening, closing, and transient groups. Their peak signal profile and heatmap are shown in the top right frame.

(E) Representative GO terms of the dynamic ATAC groups in (D).

(F) Jaccard similarity score of ND1 targets and 12 differential modified histone marks of different ND1 infection time points.

(G) UpSet plot showing H3K27ac CNT peaks for each time point at the ND1-binding sites. Most ND1-binding regions gain H3K27ac, and the top four sets are highlighted by different colors.

(H) Representative GO terms of correlated genes of the corresponding peak sets in (G).

(I) Schematic of the experiment design to investigate the role of histone acetyltransferases inhibitor (SGC-CBP30) in ND1-induced AtN conversion.

(J) Representative images showing the expression of H3K27ac and ND1. Yellow arrowheads indicate double-positive cells with neuronal morphology, and white arrowheads indicate H3K27ac$^-$ but ND1$^+$ cells without neuronal morphology. Scale bar: 50 μm.

(K and L) Representative images (K) and quantitation (L) revealing that treatment with SGC-CBP30 at 0–5 or 0–2 DPI sharply impaired AtN conversion while at 3–5 DPI had no effect. Scale bar: 50 μm. TUJ1$^+$ rate in DMSO: 71.7% ± 3.4%; TUJ1$^+$ rate in SGC-CBP30(D0–D5) 15.9% ± 2.7%; TUJ$^+$ rate in SGC-CBP30(D0–D2): 19.5% ± 1.9%; and TUJ1$^+$ rate in SGC-CBP30(D0–D5): 62.5% ± 5.5%. One-way ANOVA followed by Tukey's multiple comparisons test.

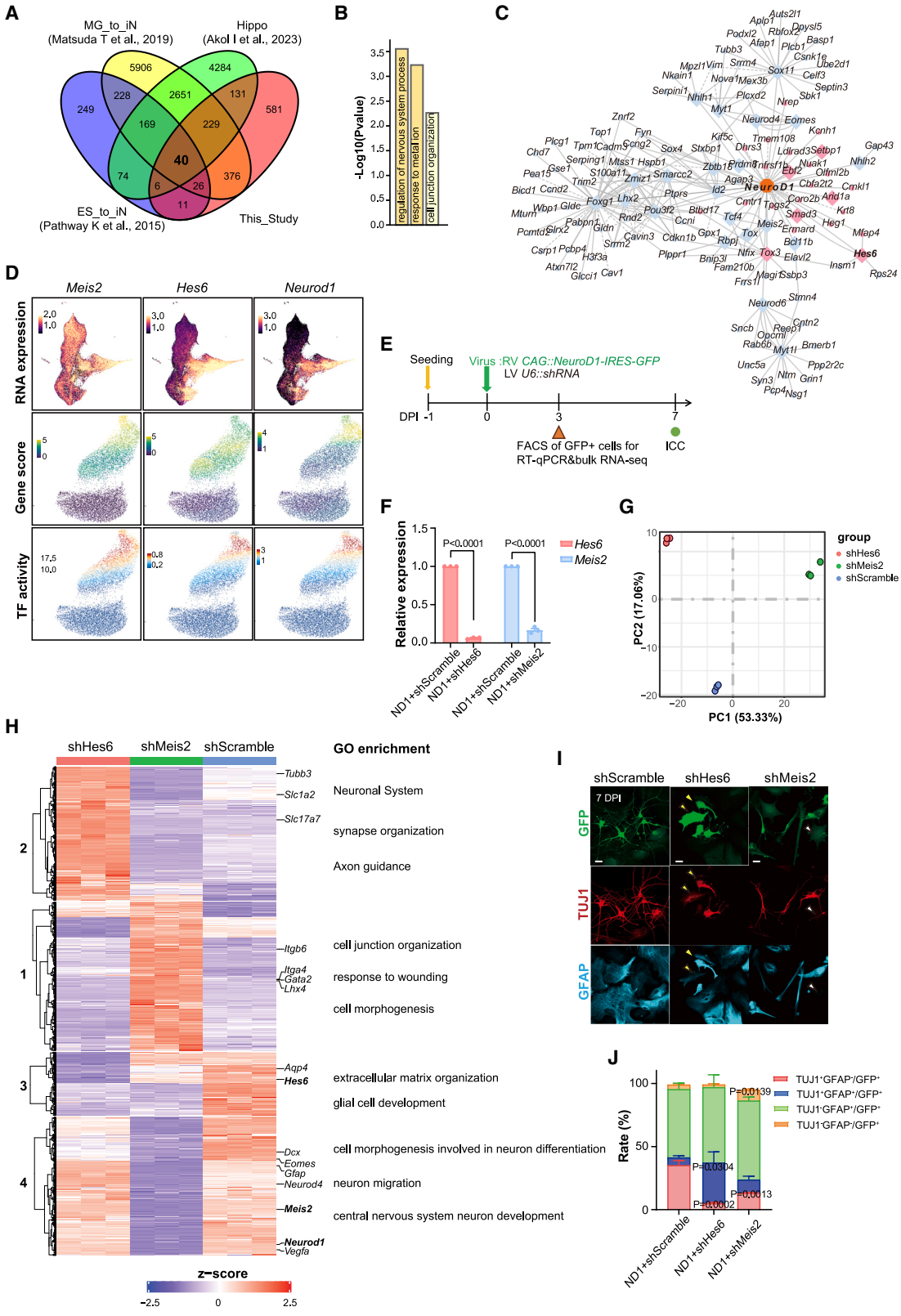

(legend on next page)

Because ND1 has been reported as a pioneer factor driving neuronal differentiation of embryonic stem cells (ESCs) or neuronal reprogramming of microglia,[22–24] we wondered whether it also worked as a pioneer factor during the AtN conversion. Thus, we analyzed the histone modification status of the ND1-preferred regions in the starting cells and investigated how they changed after ND1 binding. Among the ND1-occupied regions that had histone modifications at day 0, around half of them were modified with H3K27me3, a transcriptional repressive landmark (Figure S5C). These regions are related to genes involved in the regulation of glial cell differentiation, cell fate commitment, and neuron projection development (Figure S5D). After being bound by ND1, these H3K27me3 modifications were gradually erased (Figures S5C and S5F), supporting the role of ND1 as a pioneer TF driving the neuronal reprogramming of ImA. More frequently, the ND1-preferred regions lacked any of the detected histone modifications in ImA at day 0 (92%), which acquired the transcriptional active modifications, including H3K27ac and H3K4me3, after ND1 expression (Figure S5E). This might be the reason for the rapid induction of neuronal reprogramming of ImA by ND1 in this *in vitro* system.

To address the main histone modification changes induced by ND1, we utilized the Jaccard similarity index to analyze their temporal changes with ND1-binding sites. H3K27ac changed most consistently with ND1 binding, especially at 1 DPI (Figure 4F). Over 98% (602/612) of these ND1-binding regions gained H3K27ac modification, and 71% (434/602) of H3K27ac gained was transient within 1 and 2 DPI (Set1 and Set4) (Figure 4G). These transient H3K27ac-modified regions correspond to genes related to forebrain development, central nervous system neuron differentiation, exit from mitosis, and gliogenesis (Figure 4H). The rest of the 122 ND1-binding loci consistently gained H3K27ac modification until the late stage of 5 DPI, whose corresponding genes were enriched in the modulation of chemical synaptic transmission and axon guidance (Set2; Figures 4G and 4H). There were also 103 ND1-binding regions that gained H3K27ac modification at the late stage of 5 DPI, whose corresponding genes were involved in regulating axon guidance and negative regulation of nervous system development (Set3; Figures 4G and 4H). Together, these results indicate that ND1 remodels the chromatin landscape of neuronal genes into an accessible state through the addition of H3K27ac in a stepwise manner.

To verify the importance of H3K27ac regulation during ND1-induced AtN conversion, we added SGC-CBP30, a potent and selective inhibitor of histone acetyltransferases CBP/p300 and the ND1 retrovirus (Figure 4I). As expected, SGC-CBP30 reduced H3K27ac levels, especially in those ND1-transduced cells whose expression of ND1 was normal but still retained astrocyte morphology (Figure 4J). The inhibition of H3K27ac modification obviously hampered the conversion of astrocytes when it was added at the very early stage (0–5 or 0–2 DPI), while it failed to affect the reprogramming if added at a later stage (3–5 DPI; Figures 4K and 4L). This result is consistent with the observation that the most abundant gain of H3K27ac occurred at an early stage of the conversion.

Identification of core regulatory genes in ND1-induced neuronal reprogramming

ND1 has been reported as a highly potent factor in promoting neuronal fate specification during development and reprogramming.[22,24] Previous studies have identified thousands of ND1 targets, including cascades of critical transcriptional factors based on different contexts: ND1-induced direct neuronal differentiation from ESCs, ND1-induced neuronal reprogramming from microglia, and neurogenesis.[22–25] We wondered whether there were shared regulatory factors across ND1-induced AtN conversion and the other neuronal specifications. Thus, we reanalyzed ND1 chromatin immunoprecipitation (ChIP)-seq datasets from previous studies and compared those with our ND1 CNT data (Figure S6A and STAR Methods). 40 common genes were identified as ND1 direct targets across all ND1-driven programs (Figure 5A and Table S5). These genes were mostly enriched in the regulation of nervous system processes (Figure 5B). For example, common ND1-binding peaks were visualized in the regulatory regions of *Hes6*, *Mfap4*, and *Smad3* in all four systems (Figure S6B). *Hes6* is also a critical TF in neuronal reprogramming triggered by other neural TFs.[26,27] *Mfap4* is expressed in IPCs during neurogenesis.[28] *Smad3* is a TGF-β-pathway-related protein that maintains the stemness of NSCs.[29,30] The common ND1-targeted genes among the 4 different systems suggest common transcriptional regulation of ND1-induced neuronal

Figure 5. Critical ND1 targets involved in neuronal reprograming

(A) Venn diagram showing the overlap of ND1 targets identified in different datasets. There are 40 common target genes highlighted.

(B) Representative GO terms of the 40 common ND1 target genes.

(C) Gene regulatory network of ND1-induced AtN conversion from scRNA-seq and ND1 CNT data. Diamonds indicate TFs, and the common targets from (A) are colored pink.

(D) RNA expression from scRNA-seq and gene score and TF activity from scATAC-seq of *Meis2*, *Hes6*, and *Neurod1*.

(E) Schematic of shRNA knockdown experiment.

(F) Quantitative PCR showing that the mRNA level of *Hes6* and *Meis2* was successfully knocked down by shRNA. The expression values are normalized to the scramble group.

(G) PCA of genome-wide gene profile of each sample. GFP^+ cells were collected from ND1+shHes6 (shHes6), ND1+shMeis2 (shMeis2), and ND1+shScramble (shScramble) at 3 DPI.

(H) Heatmap of genome-wide expression analysis of three groups.

(I and J) Representative images (I) and quantitation (J) revealing that the knockdown of *Hes6* (*shHes6*) and *Meis2* (*shMeis2*) dramatically impaired ND1-induced AtN conversion. Yellow arrowheads indicate $TUJ1^+GFAP^+$ cells, and white arrowheads indicate $TUJ1^-GFAP^-$ cells. Scale bar: 50 μm. shScramble: $TUJ1^+GFAP^-/GFP^+$ = 35.1% ± 3.9%; $TUJ1^+GFAP^+/GFP^+$ = 6.2% ± 1.5%; $TUJ1^-GFAP^+/GFP^+$ = 54.1% ± 5.0%; and $TUJ1^-GFAP^-/GFP^+$ = 3.6% ± 0.9%. shHes6: $TUJ1^+GFAP^-/GFP^+$ = 4.8% ± 0.9%; $TUJ1^+GFAP^+/GFP^+$ = 32.3% ± 8.6%; $TUJ1^-GFAP^+/GFP^+$ = 59.8% ± 10.0%; and $TUJ1^-GFAP^-/GFP^+$ = 2.2% ± 0.8%. shMeis2: $TUJ1^+GFAP^-/GFP^+$ = 13.2% ± 0.4%; $TUJ1^+GFAP^+/GFP^+$ = 10.5% ± 2.9%; $TUJ1^-GFAP^+/GFP^+$ = 62.6% ± 3.0%; and $TUJ1^-GFAP^-/GFP^+$ = 8.5% ± 0.8%. One-way ANOVA followed by Tukey's multiple comparisons test.

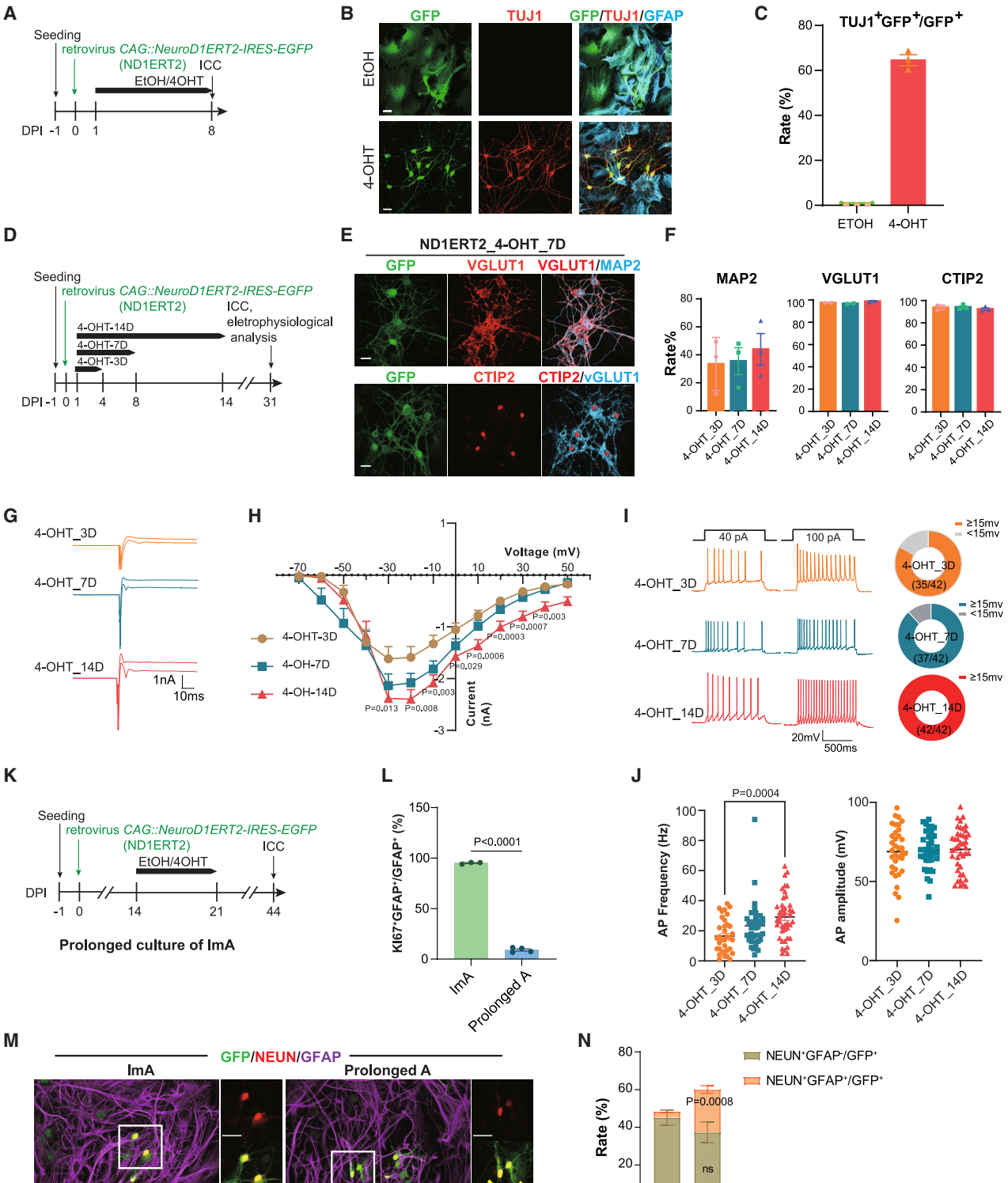

(legend on next page)

specification. Based on the scRNA-seq data, we established a gene regulation network of the ND1-induced AtN conversion and further narrowed the 40 common targets to 25 whose expression was correlated with that of ND1 (Figure 5C). 20 out of the 25 common genes were upregulated after induction, suggesting that ND1 mainly acts as a transcriptional activator during the AtN conversion (Figure S6D). There were five ND1 target genes whose expression was downregulated in the neuronal subclusters but increased in the astrocyte subclusters, suggesting that ND1 may also work to silence some astrocyte-related genes directly. Taking the TF activity measured by scATAC-seq into consideration, only *Hes6* and *Smad3* showed activity changes during our AtN conversion (Figures 5D and S6E). Besides the common core ND1 targets shared across all 4 systems, we noticed that *Meis2*, another direct ND1 target discovered in this study, had a significant TF activity increase in the converting cells (Figures 5C and 5D). *Meis2* was also an ND1 target in microglia-to-neuron transdifferentiation and neurogenesis but was not presented in the neuronal specification from ESCs (Figure S6C).

To validate the roles of *Hes6* and *Meis2* in the AtN conversion, we employed shRNA to KD their expression (Figures 5E and 5F), and conducted bulk RNA -seq to investigate what genes and pathways were affected by knocking down these genes during ND1-mediated neuronal reprogramming. The principal-component analysis (PCA) map revealed huge differences in gene expression profiles among the three groups (Figure 5G). We further extracted the differentially expressed genes (DEGs) among the three groups of cells and clustered them according to their expression patterns (Figure 5H and Table S6). The lower expression of *Hes6* and *Meis2* in the corresponding KD group indicated successful KD. *Hes6* KD directly upregulated the genes related to late neurogenesis, including neuronal system and synapse organization (e.g., *Tubb3*, *Slc1a*, *Slc17a7*, etc.; Figure 5H). These data suggest that *Hes6* KD during ND1-mediated neuronal reprogramming may directly activate the expression of neuronal genes in the astrocytes. *Meis2* KD led to the downregulation of endogenous *Neurod1*, which directly affected further gene programs governed by ND1. So, genes related to both early and late neurogenesis were no longer upregulated (Figure 5H). Immunostaining results at 7 DPI supported indispensable roles of *Hes6* and *Meis2* in ND1-induced AtN conversion, as we observed that both *Hes6* and *Meis2* KDs significantly reduced ND1-induced AtN efficiency (Figures 5I and 5J). Notably, when *Hes6* was knocked down, a significantly higher percentage of TUJ1$^+$/GFAP$^+$ cells was observed (Figures 5I and 5J). These collective results suggest that *Hes6* and *Meis2* play different roles during ND1-induced AtN.

Taking these results together, through the integrative analysis across different neuronal specification systems induced by ND1, we identified the core genes directly regulated by ND1, which activated the neuronal transcriptional program and silenced the astrocytic transcriptional program.

Transient expression of exogenous ND1 in the astrocytes is sufficient to initiate the neuronal program

The *CAG* promoter is a constitutive promoter that drives the expression of exogenous ND1 during the whole process of AtN conversion. The total and endogenous ND1 expression was

Figure 6. Transient activation of exogenous ND1 induces neuronal fate commitment

(A) Schematic of experiment design to validate that the ND1ERT2 system efficiently converted astrocytes to neurons.

(B and C) Representative images (B) and quantitation (C) showing the AtN conversion after transduction with the retrovirus ND1ERT2 (GFP, green) and the supplement of 4-OHT or EtOH. TUJ1$^+$ rate in ETOH group: 0.0% ± 0.0%; TUJ1$^+$ rate in 4-OHT group: 64.6% ± 2.4%. Scale bar: 20 μm.

(D) Schematic of experiment design to compare the AtN efficiencies under different 4-OHT treatment periods.

(E and F) Representative images (E) and quantitation (F) revealing the AtN efficiency (indicated by MAP2 in cyan) and the proportion of the neuronal subtypes of the converted neurons (indicated by VGLUT1 in red on the top and in cyan on the bottom of E and by CTIP2 in red) after transduction with the retrovirus ND1ERT2 (GFP, green) and the supplement of 4-OHT at different time periods (4-OHT_3D, 4-OHT_7D, and 4-OHT_14D). Scale bar: 20 μm. MAP2$^+$ rates: 4-OHT_3D = 26.9% ± 7.7%; 4-OHT_7D = 29.0% ± 6.3%; and 4-OHT_14D = 35.8% ± 7.2%. VGLUT1$^+$ rates: 4-OHT_3D = 97.5% ± 0.1%; 4-OHT_7D = 96.8% ± 0.2%; and 4-OHT_14D = 98.7% ± 0.9%. CTIP2$^+$ rates: 4-OHT_3D = 93.8% ± 1.2%; 4-OHT_7D = 94.1% ± 1.2%; and 4-OHT_14D = 92.3% ± 1.2%. One-way ANOVA followed by Tukey's multiple comparisons test.

(G and H) Representative traces (G) and quantitation (H) of the sodium current of the converted neurons after different treatment periods of 4-OHT. Sodium current (injection voltage): 4-OHT-3D = −0.03 ± 0.02 nA (−70 mV); −0.03 ± 0.03 nA (−60 mV); −0.52 ± 0.19 nA (−50 mV); −1.42 ± 0.23 nA (−40 mV); −1.71 ± 0.23 nA (−30 mV); −1.49 ± 0.19 nA (−20 mV); −1.20 ± 0.15 nA (−10 mV); −0.95 ± 0.12 nA (0 mV); −0.68 ± 0.09 nA (10 mV); −0.41 ± 0.07 nA (20 mV); −0.29 ± 0.06 nA (30 mV); −0.2 ± 0.05 nA (40 mV); and −0.14 ± 0.05 nA (50 mV). 4-OHT-7D = −0.05 ± 0.05 nA (−70 mV); −0.51 ± 0.22 nA (−60 mV); −1.06 ± 0.3 nA (−50 mV); −1.81 ± 0.26 nA (−40 mV); −2.27 ± 0.21 nA (−30 mV); −2.02 ± 0.18 nA (−20 mV); −1.69 ± 0.15 nA (−10 mV); −1.2 ± 0.13 nA (0 mV); −0.90 ± 0.11 nA (10 mV); −0.60 ± 0.09 nA (20 mV); −0.37 ± 0.08 nA (30 mV); −0.18 ± 0.09 nA (40 mV); and −0.15 ± 0.05 nA (40 mV). 4-OHT-14D = 0.00 ± 0.00 nA (−70 mV); −0.07 ± 0.05 nA (−60 mV); −0.52 ± 0.20 nA (−50 mV); −2.00 ± 0.29 nA (−40 mV); −2.6 ± 0.21 nA (−30 mV); −2.27 ± 0.17 nA (−20 mV); −1.9 ± 0.14 nA (−10 mV); −1.45 ± 0.15 nA (0 mV); −1.24 ± 0.11 nA (10 mV); −0.93 ± 0.11 nA (20 mV); −0.73 ± 0.11 nA (30 mV); −0.57 ± 0.10 nA (40 mV); and −0.20 ± 0.06 nA (50 mV). n = 42 converted neurons/group from 3 independent experiments; one-way ANOVA followed by Tukey's multiple comparisons test.

(I) Representative traces and statistical analysis of repetitive action potential (AP) fired by the converted neurons after different treatment periods of 4-OHT.

(J and L) Statistical analysis of the frequencies (J) and amplitudes (L) of the AP fired by the converted neurons after different treatment periods of 4-OHT. AP frequency: 4-OHT-3D = 16.54 ± 1.87 Hz, 4-OHT-7D = 23.38 ± 2.53 Hz, and 4-OHT-14D = 29.79 ± 2.28 Hz. AP amplitude: 4-OHT-3D = 68.88 ± 2.72 mV, 4-OHT-7D = 69.87 ± 1.87 mV, and 4-OHT-14D = 70.26 ± 2.10 mV. n = 42 converted neurons/group from 3 independent experiments; one-way ANOVA followed by Tukey's multiple comparisons test.

(K) Schematic of experimental design to investigate the capacity of ND1 to convert prolonged culture astrocytes.

(L) Histogram revealing rare proliferative cells in the prolonged astrocytes (prolonged A). ImA, immature astrocytes. KI67$^+$GFAP$^+$/GFAP$^+$: ImA = 95.1% ± 0.5%, prolonged A = 9.1% ± 1.2%. Unpaired t test.

(M and N) Representative images (M) and quantitation (N) revealing comparable ND1-induced AtN conversion efficiency (indicated by NEUN$^+$GFAP$^-$) between ImA and prolonged cultures. Scale bars: 50 μm and 25 μm. ImA: NEUN$^+$GFAP$^-$/GFP$^+$ = 45.2% ± 4.0% and NEUN$^+$GFAP$^+$/GFP$^+$ = 3.3% ± 0.8%; prolonged A: NEUN$^+$GFAP$^-$/GFP$^+$ = 37.3% ± 5.5% and NEUN$^+$GFAP$^+$/GFP$^+$ = 22.8% ± 2.0%. Unpaired t test.

detected by qPCR 24 h after transduction (Figure S7A). Ectopic ND1 induced the upregulation of endogenous core TFs, including *endoNeuroD1* and *Hes6*, to activate the transcriptional program of neuronal specification. Therefore, we wondered how long was required for the ectopic ND1 to complete neural reprogramming. To control the activation of exogenous ND1, we induced a conditional ectopic ND1 expression system by including ERT2 in the retrovirus (hereafter indicated as ND1ERT2). A FLAG tag was added to the N terminus of ND1 to discriminate the exogenous ND1. The exogenous ND1 was detectable 24 h after the addition of 4-hydroxy-tamoxifen (4-OHT) (Figure S7B). In the control group with added ethanol (EtOH), no TUJ1$^+$ neurons were generated after 1 week, while 4-OHT treatment converted about 60% of astrocytes into TUJ1$^+$ neurons (Figures 6A–6C). Then, we treated the ND1ERT2-transduced astrocytes with 4-OHT for 3, 7, and 14 days, respectively, to explore the shortest period of exogenous ND1 acquisition (Figure 6D). Consistent with the previous CAG::ND1-induced AtN conversion program (Figure 2), 3-day treatment with 4-OHT induced astrocytes to the intermediate state co-expressing GFAP and EOMES, while 7-day treatment converted them to TUJ1$^+$ neurons expressing CTIP2 (Figure S7C). MAP2$^+$ neurons with weak expression of VGLUT1 were observed in the 14-day treatment of cells (Figure S7C). When analyzing the conversion rate and the subtypes of converted neurons 30 days after the 4-OHT supplement, almost all converted cells belonged to the neuronal subtype expressing VGLUT1 and CTIP2 (Figure 6E). Quantitatively, there was no significant difference in the conversion rates of MAP2 neurons among different 4-OHT treatment time groups (Figure 6F). These results indicate that transient activation of exogenous ND1 in the astrocytes is sufficient to trigger complete neuronal conversion.

Although the conversion rates and the converted neuronal subtypes were similar, the neurons induced with 14-day 4-OHT treatment displayed significantly higher resting membrane potential (RMP) and more robust sodium currents compared with those with 3-day 4-OHT treatment (Figures 6G and S7E). Consistently, the former converted neurons had significantly bigger soma size and higher membrane capacitance (Figures S7D, S7F, and S7G). In addition, neurons converted after long-term treatment with 4-OHT had higher rates of firing repetitive action potentials with elevated frequency compared with the neurons converted after short-term treatment with 4-OHT (Figures 6I and 6J). These data implied that although short-term induction of exogenous ND1 is sufficient to trigger astrocyte-to-neuron reprogramming, long-term activation of exogenous ND1 could facilitate the converted neuron to acquire more mature electrophysiological features.

ND1 reprograms non-diving astrocytes to neurons as well

Since the ImAs became mature upon the prolonged culture, with decreased cell proliferation ability and increased expression of astrocyte markers (Figures 1H, S3, 6L, and S7H), we further evaluated the ability of ND1 to convert the prolonged cultures into neurons by treating the ND1ERT2-transduced astrocytes with 4-OHT after culturing them for 2 weeks. At day 30 after 4-OHT induction, we calculated the rate of AtN conversion (Figure 6K). ND1 could also convert the prolonged cultures of ImAs into neurons with comparable efficiency to its conversion of ImAs (indicated by NEUN$^+$GFAP$^-$, Figures 6M and 6N), but the rate of NEUN$^+$GFAP$^+$ cells was significantly higher, suggesting a longer time required for ND1 to convert the prolonged cultures into neurons (Figures 6M and 6N).

DISCUSSION

Previous studies have reported direct and indirect paths of neuronal reprogramming. The direct neuronal reprogramming bypasses the NSC state, while in the indirect path, astrocytes undergo de-differentiation into transiently amplifying cells that express ASCL1, which then further differentiate into neuroblasts.[31,32] In our ND1-induced AtN conversion, we observed a different pattern from the previous two paths. Upon the stimulation of ND1, the astrocytes entered a transient intermediate state with simultaneous activation of both astrocytic and IPC genes and then quickly passed this intermediate stage to acquire neuronal fate. The intermediate stage of IPC-like cells discovered in this study has also been implicated in a previous study using bulk RNA-seq to dissect ND1-induced neuronal reprogramming of human primary astrocytes, which reported the activation of IPC-enriched genes *MFAP4* and *SSTR2* in the early stage.[17] This suggests a conserved trajectory of ND1-induced AtN conversion among different species. The intermediate state between the parental cells and IPCs has seldom been reported in other neuronal reprogramming systems.[8,18,20,33] The cultured astrocytes remained as ImAs with high proliferation ability,[34] and in the absence of pro-neuronal TFs, they would gradually mature under prolonged culture, as revealed by the astrocyte branch in our pseudotime analysis. This default program of astrocyte maturation might not be immediately shut down by the exogenous ND1. As shown in our and previous studies, ND1 acts mainly as a transcriptional activator to increase the chromatin accessibility of the regulatory regions corresponding to genes related to neurogenesis, including *Hes6*.[22–24] The elevation of *Hes6* has been reported in neuronal reprogramming induced by other TFs or Notch signaling depletion both *in vitro* and *in vivo*,[8,18,20,27] but its role has not been elucidated. We found that *Hes6* KD during ND1-mediated AtN enabled the astrocytes to express genes related to late neurogenesis as early as 3 days, while the neural progenitor genes decreased, suggesting that ND1 may act through *Hes6* to push astrocytes into the IPC stage. However, ND1-transduced astrocytes in the absence of *Hes6* failed to be converted to neurons, suggesting the necessity of the transient IPC stage during ND1-induced neuronal reprogramming of ImAs. Besides the activation of the neuronal program, ND1 also requires downstream effectors to repress astrocyte genes. We first thought it might be *Meis2*, as it has been reported to silence the glial genes in ND1-induced microglia-to-neuron conversion.[24] But our data showed that *Meis2* KD led to the failure of the activation of the neural transcriptional program induced by ND1. More interestingly, the endogenous *Neurod1* was shut down after *Meis2* KD. These results suggest that *Meis2* may serve as an important regulator for ND1.

Once the neurogenic program is initiated, this ND1-induced AtN conversion recapitulates the transcriptional progress of

cortical deep-layer neurogenesis, passing through RG cell, IPC, and migrating neuron states. Probably because of the high similarity between these two programs, ND1-converted neurons shared the characteristics of primary cortical deep-layer neurons both in gene expression and electrophysiological features. This is the first time that a continuous cellular trajectory has been established to describe the reprogramming path of ND1-induced AtN conversion and its relationship with endogenous neuronal development. Besides the similarity, there are some features unique to ND1-induced AtN conversion. For example, the pathways involved in the response to oxidative stress and innate immune response are activated during ND1-induced AtN conversion. The activation of the stress and innate immune signal during cell fate switch has been reported previously,[35,36] which was reported to be necessary for successful reprogramming. These studies (including this study) suggest that the activation of immune and inflammatory signals may be a common phenomenon, but the role of the immune and inflammatory signals in AtN conversion requires future investigation.

Multiomics analyses reveal that ND1 directly binds the regulatory regions of pro-neuronal genes to increase chromatin accessibility and upregulates their expression, suggesting that ND1 predominantly acts as an activator of the neurogenic program. Through CNT analysis, we discovered that ND1 reshaped the open chromatin landscapes of the ImAs mainly through gaining H3K27ac. The increase of H3K27ac upon ND1 expression has been reported in the direct neuronal induction of pluripotent stem cells,[22,23] which is not evident during ND1-induced neuronal reprogramming from microglia.[24] The difference in histone modification indicates that the mode of how ND1 remodels the histone modification patterns of start cells is context dependent. Besides, we also found that ND1 could bind loci modified with H3K27me3 and erased this modification.[22–24] This feature supports ND1 as a pioneer TF to drive AtN conversion, which is also observed in the direct neuronal specification induced by ND1 from ESCs and microglia, suggesting the common role of ND1. Meanwhile, the dose of overexpressed ND1 is very important, as the successful clusters (Neu_3 and Neu_4) expressed much higher levels of *EGFP* versus unsuccessful clusters (Ast1-2-3) from ND1-EGFP$^+$ cells. The successful clusters also highly expressed genes related to chromatin organization (data not shown), indicating that chromatin remodeling might be a bottleneck for reprogramming. Specifically, *Eomes*, as an IPC marker, also cooperates with the switch/sucrose non-fermentable (SWI/SNF) complex to drive chromatin rewiring.[37] We proved that knocking down *Eomes* absolutely abolished reprogramming.

Limitations of the study

This study also has some limitations. One is that the analysis is based on an *in vitro* AtN conversion system and may be different from the mechanisms of *in vivo* ND1-induced AtN conversion. Nevertheless, the time course and the conversion rate in this system are similar to the previous *in vivo* study converting the dividing astrocytes under injury or disease conditions into functional neurons.[16] Thus, the regulations uncovered in this study may help to explain how ND1 triggers dividing astrocytes *in vivo* to transdifferentiate into neurons. Another limitation is that the start cells in this study are proliferative ImAs (and we did not fully assess whether the starting population was free of RG cells), whose number is quite limited *in vivo*.[38,39] Many pieces of evidence are presented that proliferative reactive astrocytes are more plastic than non-proliferative reactive astrocytes.[40–42] In most cases, they may be easy to reprogram by ND1, as it has been shown in this study that the majority of ND1 target loci are null of histone modifications. The epigenetic landscape of the non-proliferative astrocytes and how it is dynamically changed upon ND1 overexpression require future exploration.

RESOURCE AVAILABILITY

Lead contact

Requests for further information and resources should be directed to and will be fulfilled by the lead contact, Xiaoying Fan (fan_xiaoying@gzlab.ac.cn).

Materials availability

This study did not generate new materials.

Data and code availability

The raw data used in this paper have been deposited to the Genome Sequence Archive in National Genomics Data Center, and the accession numbers are listed in the key resources table. All code used in this study is available in the GitHub repository, and the link is provided in the key resources table. Any additional information required to reanalyze the data reported in this paper is available from the lead contact upon request.

ACKNOWLEDGMENTS

This work is supported by grants from the National Key Research and Development Program of China (2020YFA0112201 to X.F.), the Key Research and Development Program of Guangzhou (202206060002 to X.F., W.L., and G.C.), the Guangdong Provincial Pearl River Talents Program (2021QN02Y747 to X.F.), the Natural Science Foundation of Guangdong Province of China (2023A1515011719 to W.L.), and the Pearl River Innovation and Entrepreneurship Team (2021ZT09Y552 to G.C.).

AUTHOR CONTRIBUTIONS

X.F., W.L., and G.C. conceived the ideas. X.F. and W.L. supervised the project. W.L. and K.L. established the *in vitro* neuronal reprogramming platform, collected the data, and finished the analyses, except for the sequencing experiments, with the assistance of D.S. D.S. performed all the single-cell, CUT&Tag, and RNA-seq experiments, and X. Li conducted the bioinformatics analyses. Q.H. did the RT-qPCR validation experiments. J.Z. collected electrophysiology data. X. Luo constructed the retroviral vectors. X.F., W.L., and D.S. wrote the manuscript, and all authors discussed the data. X.F., G.C., and W.L. proofread the manuscript.

DECLARATION OF INTERESTS

G.C. is a co-founder of NeuExcell Therapeutics, Inc.

STAR★METHODS

Detailed methods are provided in the online version of this paper and include the following:

- KEY RESOURCES TABLE
- METHOD DETAILS
  - Experimental model and study participant details
  - Primary cell culture
  - Retrovirus production
  - *In vitro* AtN conversion

- RNA interference
- Immunofluorescence
- Electrophysiological recording
- Single-cell suspension acquisition
- CUT&Tag experiments
- scRNA-seq and scATAC-seq library preparation and sequencing
- Bulk RNA-seq experiments
- scRNA-seq data analysis
- Trajectory analysis
- Key transcription factor analysis
- WGCNA analysis
- Mapping *in vitro* cells to *in vivo* references
- scATAC-seq data analysis
- CUT&Tag data processing
- Inferring ND1 target genes and ND1 network using CUT&Tag and scRNA-seq data
- RNA-seq data preprocessing

- QUANTIFICATION AND STATISTICAL ANALYSIS
  - Immunofluorescence analysis
  - Real-time qPCR analysis

SUPPLEMENTAL INFORMATION

Supplemental information can be found online at https://doi.org/10.1016/j.celrep.2025.115523.

Received: June 28, 2024
Revised: February 3, 2025
Accepted: March 14, 2025
Published: April 1, 2025

REFERENCES

1. Kempermann, G., Gage, F.H., Aigner, L., Song, H., Curtis, M.A., Thuret, S., Kuhn, H.G., Jessberger, S., Frankland, P.W., Cameron, H.A., et al. (2018). Human Adult Neurogenesis: Evidence and Remaining Questions. Cell Stem Cell. *23*, 25–30. https://doi.org/10.1016/j.stem.2018.04.004.
2. Lei, W., Li, W., Ge, L., and Chen, G. (2019). Non-engineered and Engineered Adult Neurogenesis in Mammalian Brains. Front. Neurosci. *13*, 131. https://doi.org/10.3389/fnins.2019.00131.
3. Vasan, L., Park, E., David, L.A., Fleming, T., and Schuurmans, C. (2021). Direct Neuronal Reprogramming: Bridging the Gap Between Basic Science and Clinical Application. Front. Cell Dev. Biol. *9*, 681087. https://doi.org/10.3389/fcell.2021.681087.
4. Bocchi, R., Masserdotti, G., and Götz, M. (2022). Direct neuronal reprogramming: Fast forward from new concepts toward therapeutic approaches. Neuron *110*, 366–393. https://doi.org/10.1016/j.neuron.2021.11.023.
5. Burda, J.E., and Sofroniew, M.V. (2014). Reactive gliosis and the multicellular response to CNS damage and disease. Neuron *81*, 229–248. https://doi.org/10.1016/j.neuron.2013.12.034.
6. Robel, S., Berninger, B., and Götz, M. (2011). The stem cell potential of glia: lessons from reactive gliosis. Nat. Rev. Neurosci. *12*, 88–104. https://doi.org/10.1038/nrn2978.
7. Magnusson, J.P., Göritz, C., Tatarishvili, J., Dias, D.O., Smith, E.M.K., Lindvall, O., Kokaia, Z., and Frisén, J. (2014). A latent neurogenic program in astrocytes regulated by Notch signaling in the mouse. Science *346*, 237–241. https://doi.org/10.1126/science.346.6206.237.
8. Zamboni, M., Llorens-Bobadilla, E., Magnusson, J.P., and Frisén, J. (2020). A Widespread Neurogenic Potential of Neocortical Astrocytes Is Induced by Injury. Cell Stem Cell. *27*, 605–617.e5. https://doi.org/10.1016/j.stem.2020.07.006.
9. Tai, W., Wu, W., Wang, L.L., Ni, H., Chen, C., Yang, J., Zang, T., Zou, Y., Xu, X.M., and Zhang, C.L. (2021). In vivo reprogramming of NG2 glia enables adult neurogenesis and functional recovery following spinal cord injury. Cell Stem Cell. *28*, 923–937.e4. https://doi.org/10.1016/j.stem.2021.02.009.
10. Ge, L.J., Yang, F.H., Li, W., Wang, T., Lin, Y., Feng, J., Chen, N.H., Jiang, M., Wang, J.H., Hu, X.T., and Chen, G. (2020). In vivo Neuroregeneration to Treat Ischemic Stroke Through NeuroD1 AAV-Based Gene Therapy in Adult Non-human Primates. Front. Cell Dev. Biol. *8*, 590008. https://doi.org/10.3389/fcell.2020.590008.
11. Wu, Z., Parry, M., Hou, X.Y., Liu, M.H., Wang, H., Cain, R., Pei, Z.F., Chen, Y.C., Guo, Z.Y., Abhijeet, S., and Chen, G. (2020). Gene therapy conversion of striatal astrocytes into GABAergic neurons in mouse models of Huntington's disease. Nat. Commun. *11*, 1105. https://doi.org/10.1038/s41467-020-14855-3.
12. Zheng, J., Li, T., Qi, S., Qin, B., Yu, J., and Chen, G. (2022). Neuroregenerative gene therapy to treat temporal lobe epilepsy in a rat model. Prog. Neurobiol. *208*, 102198. https://doi.org/10.1016/j.pneurobio.2021.102198.
13. Chen, Y.C., Ma, N.X., Pei, Z.F., Wu, Z., Do-Monte, F.H., Keefe, S., Yellin, E., Chen, M.S., Yin, J.C., Lee, G., et al. (2020). A NeuroD1 AAV-Based Gene Therapy for Functional Brain Repair after Ischemic Injury through In Vivo Astrocyte-to-Neuron Conversion. Mol. Ther. *28*, 217–234. https://doi.org/10.1016/j.ymthe.2019.09.003.
14. Hevner, R.F., Hodge, R.D., Daza, R.A.M., and Englund, C. (2006). Transcription factors in glutamatergic neurogenesis: conserved programs in neocortex, cerebellum, and adult hippocampus. Neurosci. Res. *55*, 223–233. https://doi.org/10.1016/j.neures.2006.03.004.
15. Gao, Z., Ure, K., Ables, J.L., Lagace, D.C., Nave, K.A., Goebbels, S., Eisch, A.J., and Hsieh, J. (2009). Neurod1 is essential for the survival and maturation of adult-born neurons. Nat. Neurosci. *12*, 1090–1092. https://doi.org/10.1038/nn.2385.
16. Guo, Z., Zhang, L., Wu, Z., Chen, Y., Wang, F., and Chen, G. (2014). In vivo direct reprogramming of reactive glial cells into functional neurons after brain injury and in an Alzheimer's disease model. Cell Stem Cell. *14*, 188–202. https://doi.org/10.1016/j.stem.2013.12.001.
17. Ma, N.X., Puls, B., and Chen, G. (2022). Transcriptomic analyses of NeuroD1-mediated astrocyte-to-neuron conversion. Dev. Neurobiol. *82*, 375–391. https://doi.org/10.1002/dneu.22882.
18. Magnusson, J.P., Zamboni, M., Santopolo, G., Mold, J.E., Barrientos-Somarribas, M., Talavera-Lopez, C., Andersson, B., and Frisén, J. (2020). Activation of a neural stem cell transcriptional program in parenchymal astrocytes. Elife *9*, e59733. https://doi.org/10.7554/eLife.59733.
19. Niu, W., Zang, T., Zou, Y., Fang, S., Smith, D.K., Bachoo, R., and Zhang, C.L. (2013). In vivo reprogramming of astrocytes to neuroblasts in the adult brain. Nat. Cell Biol. *15*, 1164–1175. https://doi.org/10.1038/ncb2843.
20. Zhang, Y., Li, B., Cananzi, S., Han, C., Wang, L.L., Zou, Y., Fu, Y.X., Hon, G.C., and Zhang, C.L. (2022). A single factor elicits multilineage reprogramming of astrocytes in the adult mouse striatum. Proc. Natl. Acad. Sci. USA *119*, e2107339119. https://doi.org/10.1073/pnas.2107339119.
21. Hsiung, C.C.S., Morrissey, C.S., Udugama, M., Frank, C.L., Keller, C.A., Baek, S., Giardine, B., Crawford, G.E., Sung, M.H., Hardison, R.C., and Blobel, G.A. (2015). Genome accessibility is widely preserved and locally modulated during mitosis. Genome Res. *25*, 213–225. https://doi.org/10.1101/gr.180646.114.
22. Pataskar, A., Jung, J., Smialowski, P., Noack, F., Calegari, F., Straub, T., and Tiwari, V.K. (2016). NeuroD1 reprograms chromatin and transcription factor landscapes to induce the neuronal program. EMBO J. *35*, 24–45. https://doi.org/10.15252/embj.201591206.
23. Singh, A., Mahesh, A., Noack, F., Cardoso de Toledo, B., Calegari, F., and Tiwari, V.K. (2022). Tcf12 and NeuroD1 cooperatively drive neuronal migration during cortical development. Development *149*, dev200250. https://doi.org/10.1242/dev.200250.
24. Matsuda, T., Irie, T., Katsurabayashi, S., Hayashi, Y., Nagai, T., Hamazaki, N., Adefuin, A.M.D., Miura, F., Ito, T., Kimura, H., et al. (2019). Pioneer Factor NeuroD1 Rearranges Transcriptional and Epigenetic Profiles to

Execute Microglia-Neuron Conversion. Neuron *101*, 472–485.e7. https://doi.org/10.1016/j.neuron.2018.12.010.

25. Akol, I., Izzo, A., Gather, F., Strack, S., Heidrich, S., Ó hAilín, D., Villarreal, A., Hacker, C., Rauleac, T., Bella, C., et al. (2023). Multimodal epigenetic changes and altered NEUROD1 chromatin binding in the mouse hippocampus underlie FOXG1 syndrome. Proc. Natl. Acad. Sci. USA *120*, e2122467120. https://doi.org/10.1073/pnas.2122467120.
26. Rao, Z., Wang, R., Li, S., Shi, Y., Mo, L., Han, S., Yuan, J., Jing, N., and Cheng, L. (2021). Molecular Mechanisms Underlying Ascl1-Mediated Astrocyte-to-Neuron Conversion. Stem Cell Rep. *16*, 534–547. https://doi.org/10.1016/j.stemcr.2021.01.006.
27. Masserdotti, G., Gillotin, S., Sutor, B., Drechsel, D., Irmler, M., Jørgensen, H.F., Sass, S., Theis, F.J., Beckers, J., Berninger, B., et al. (2015). Transcriptional Mechanisms of Proneural Factors and REST in Regulating Neuronal Reprogramming of Astrocytes. Cell Stem Cell. *17*, 74–88. https://doi.org/10.1016/j.stem.2015.05.014.
28. Yuzwa, S.A., Borrett, M.J., Innes, B.T., Voronova, A., Ketela, T., Kaplan, D.R., Bader, G.D., and Miller, F.D. (2017). Developmental Emergence of Adult Neural Stem Cells as Revealed by Single-Cell Transcriptional Profiling. Cell Rep. *21*, 3970–3986. https://doi.org/10.1016/j.celrep.2017.12.017.
29. Estarás, C., Akizu, N., García, A., Beltrán, S., de la Cruz, X., and Martínez-Balbás, M.A. (2012). Genome-wide analysis reveals that Smad3 and JMJD3 HDM co-activate the neural developmental program. Development *139*, 2681–2691. https://doi.org/10.1242/dev.078345.
30. Bahia, R.K., Hao, X., Hassam, R., Cseh, O., Bozek, D.A., Luchman, H.A., and Weiss, S. (2023). Epigenetic and molecular coordination between HDAC2 and SMAD3-SKI regulates essential brain tumour stem cell characteristics. Nat. Commun. *14*, 5051. https://doi.org/10.1038/s41467-023-40776-y.
31. Heinrich, C., Blum, R., Gascón, S., Masserdotti, G., Tripathi, P., Sánchez, R., Tiedt, S., Schroeder, T., Götz, M., and Berninger, B. (2010). Directing astroglia from the cerebral cortex into subtype specific functional neurons. PLoS Biol. *8*, e1000373. https://doi.org/10.1371/journal.pbio.1000373.
32. Niu, W., Zang, T., Smith, D.K., Vue, T.Y., Zou, Y., Bachoo, R., Johnson, J.E., and Zhang, C.L. (2015). SOX2 reprograms resident astrocytes into neural progenitors in the adult brain. Stem Cell Rep. *4*, 780–794. https://doi.org/10.1016/j.stemcr.2015.03.006.
33. Karow, M., Camp, J.G., Falk, S., Gerber, T., Pataskar, A., Gac-Santel, M., Kageyama, J., Brazovskaja, A., Garding, A., Fan, W., et al. (2018). Direct pericyte-to-neuron reprogramming via unfolding of a neural stem cell-like program. Nat. Neurosci. *21*, 932–940. https://doi.org/10.1038/s41593-018-0168-3.
34. Lattke, M., Goldstone, R., Ellis, J.K., Boeing, S., Jurado-Arjona, J., Marichal, N., MacRae, J.I., Berninger, B., and Guillemot, F. (2021). Extensive transcriptional and chromatin changes underlie astrocyte maturation in vivo and in culture. Nat. Commun. *12*, 4335. https://doi.org/10.1038/s41467-021-24624-5.
35. Lee, J., Sayed, N., Hunter, A., Au, K.F., Wong, W.H., Mocarski, E.S., Pera, R.R., Yakubov, E., and Cooke, J.P. (2012). Activation of Innate Immunity Is Required for Efficient Nuclear Reprogramming. Cell *151*, 547–558. https://doi.org/10.1016/j.cell.2012.09.034.
36. Zhang, Y., Kang, Z., Liu, M., Wang, L., and Liu, F. (2024). Single-cell omics identifies inflammatory signaling as a trans-differentiation trigger in mouse embryos. Dev. Cell *59*, 961–978.e7. https://doi.org/10.1016/j.devcel.2024.02.010.
37. Schröder, C.M., Zissel, L., Mersiowsky, S.L., Tekman, M., Probst, S., Schüle, K.M., Preissl, S., Schilling, O., Timmers, H.T.M., and Arnold, S.J. (2024). EOMES establishes mesoderm and endoderm differentiation potential through SWI/SNF-mediated global enhancer remodeling. Dev. Cell *60*, 735–748.e5. https://doi.org/10.1016/j.devcel.2024.11.014.
38. Bardehle, S., Krüger, M., Buggenthin, F., Schwausch, J., Ninkovic, J., Clevers, H., Snippert, H.J., Theis, F.J., Meyer-Luehmann, M., Bechmann, I., et al. (2013). Live imaging of astrocyte responses to acute injury reveals selective juxtavascular proliferation. Nat. Neurosci. *16*, 580–586. https://doi.org/10.1038/nn.3371.
39. Frik, J., Merl-Pham, J., Plesnila, N., Mattugini, N., Kjell, J., Kraska, J., Gómez, R.M., Hauck, S.M., Sirko, S., and Götz, M. (2018). Cross-talk between monocyte invasion and astrocyte proliferation regulates scarring in brain injury. EMBO Rep. *19*, e45294. https://doi.org/10.15252/embr.201745294.
40. Gotz, M., Sirko, S., Beckers, J., and Irmler, M. (2015). Reactive astrocytes as neural stem or progenitor cells: In vivo lineage, In vitro potential, and Genome-wide expression analysis. Glia *63*, 1452–1468. https://doi.org/10.1002/glia.22850.
41. Sirko, S., Schichor, C., Della Vecchia, P., Metzger, F., Sonsalla, G., Simon, T., Bürkle, M., Kalpazidou, S., Ninkovic, J., Masserdotti, G., et al. (2023). Injury-specific factors in the cerebrospinal fluid regulate astrocyte plasticity in the human brain. Nat. Med. *29*, 3149–3161. https://doi.org/10.1038/s41591-023-02644-6.
42. Brulet, R., Zhu, J., Aktar, M., Hsieh, J., and Cho, K.O. (2017). Mice with conditional NeuroD1 knockout display reduced aberrant hippocampal neurogenesis but no change in epileptic seizures. Exp. Neurol. *293*, 190–198. https://doi.org/10.1016/j.expneurol.2017.04.005.
43. Dobin, A., Davis, C.A., Schlesinger, F., Drenkow, J., Zaleski, C., Jha, S., Batut, P., Chaisson, M., and Gingeras, T.R. (2013). STAR: ultrafast universal RNA-seq aligner. Bioinformatics *29*, 15–21. https://doi.org/10.1093/bioinformatics/bts635.
44. Liao, Y., Smyth, G.K., and Shi, W. (2014). featureCounts: an efficient general purpose program for assigning sequence reads to genomic features. Bioinformatics *30*, 923–930. https://doi.org/10.1093/bioinformatics/btt656.
45. McGinnis, C.S., Murrow, L.M., and Gartner, Z.J. (2019). DoubletFinder: Doublet Detection in Single-Cell RNA Sequencing Data Using Artificial Nearest Neighbors. Cell Syst. *8*, 329–337.e4. https://doi.org/10.1016/j.cels.2019.03.003.
46. Hao, Y., Hao, S., Andersen-Nissen, E., Mauck, W.M., 3rd, Zheng, S., Butler, A., Lee, M.J., Wilk, A.J., Darby, C., Zager, M., et al. (2021). Integrated analysis of multimodal single-cell data. Cell *184*, 3573–3587.e29. https://doi.org/10.1016/j.cell.2021.04.048.
47. Yu, G., Wang, L.G., Han, Y., and He, Q.Y. (2012). clusterProfiler: an R package for comparing biological themes among gene clusters. OMICS *16*, 284–287. https://doi.org/10.1089/omi.2011.0118.
48. Cao, J., Spielmann, M., Qiu, X., Huang, X., Ibrahim, D.M., Hill, A.J., Zhang, F., Mundlos, S., Christiansen, L., Steemers, F.J., et al. (2019). The single-cell transcriptional landscape of mammalian organogenesis. Nature *566*, 496–502. https://doi.org/10.1038/s41586-019-0969-x.
49. Qiu, X., Mao, Q., Tang, Y., Wang, L., Chawla, R., Pliner, H.A., and Trapnell, C. (2017). Reversed graph embedding resolves complex single-cell trajectories. Nat. Methods *14*, 979–982. https://doi.org/10.1038/nmeth.4402.
50. Lachmann, A., Giorgi, F.M., Lopez, G., and Califano, A. (2016). ARACNe-AP: gene network reverse engineering through adaptive partitioning inference of mutual information. Bioinformatics *32*, 2233–2235. https://doi.org/10.1093/bioinformatics/btw216.
51. Samuel Morabito, F.R., Rahimzadeh, N., and Miyoshi, E.; View ORCID ProfileVivek Swarup (2022). High dimensional co-expression networks enable discovery of transcriptomic drivers in complex biological systems. Preprint at bioRxiv. https://doi.org/10.1101/2022.09.22.509094.
52. Brunson, J.C. (2020). ggalluvial: Layered Grammar for Alluvial Plots. J. Open Source Softw. *5*, 2017. https://doi.org/10.21105/joss.02017.
53. Granja, J.M., Corces, M.R., Pierce, S.E., Bagdatli, S.T., Choudhry, H., Chang, H.Y., and Greenleaf, W.J. (2021). ArchR is a scalable software package for integrative single-cell chromatin accessibility analysis. Nat. Genet. *53*, 403–411. https://doi.org/10.1038/s41588-021-00790-6.
54. Feng, J., Liu, T., and Zhang, Y. (2011). Using MACS to identify peaks from ChIP-Seq data. Curr Protoc Bioinformatics. *Chapter 2*, 2.14.1–2.14.14. https://doi.org/10.1002/0471250953.bi0214s34.

55. Schep, A.N., Wu, B., Buenrostro, J.D., and Greenleaf, W.J. (2017). chromVAR: inferring transcription-factor-associated accessibility from single-cell epigenomic data. Nat. Methods *14*, 975–978. https://doi.org/10.1038/nmeth.4401.

56. Andrews, S. (2010). FastOC: A guality control tool for high throughput sequence data. https://www.bioinformatics.babraham.ac.uk/projects/fastqc/.

57. Li, B., and Dewey, C.N. (2011). RSEM: accurate transcript quantification from RNA-Seq data with or without a reference genome. BMC Bioinf. *12*, 323. https://doi.org/10.1186/1471-2105-12-323.

58. Love, M.I., Huber, W., and Anders, S. (2014). Moderated estimation of fold change and dispersion for RNA-seq data with DESeq2. Genome Biol. *15*, 550. https://doi.org/10.1186/s13059-014-0550-8.

59. McCarthy, K.D., and de Vellis, J. (1980). Preparation of separate astroglial and oligodendroglial cell cultures from rat cerebral tissue. J. Cell Biol. *85*, 890–902.

60. Zhang, Y., Sloan, S.A., Clarke, L.E., Caneda, C., Plaza, C.A., Blumenthal, P.D., Vogel, H., Steinberg, G.K., Edwards, M.S.B., Li, G., et al. (2016). Purification and Characterization of Progenitor and Mature Human Astrocytes Reveals Transcriptional and Functional Differences with Mouse. Neuron *89*, 37–53. https://doi.org/10.1016/j.neuron.2015.11.013.

61. Deng, L., Yao, J., Fang, C., Dong, N., Luscher, B., and Chen, G. (2007). Sequential postsynaptic maturation governs the temporal order of GABAergic and glutamatergic synaptogenesis in rat embryonic cultures. J. Neurosci. *27*, 10860–10869. https://doi.org/10.1523/JNEUROSCI.2744-07.2007.

62. Qiu, X., Hill, A., Packer, J., Lin, D., Ma, Y.A., and Trapnell, C. (2017). Single-cell mRNA quantification and differential analysis with Census. Nat. Methods *14*, 309–315. https://doi.org/10.1038/nmeth.4150.

63. Khan, A., Fornes, O., Stigliani, A., Gheorghe, M., Castro-Mondragon, J.A., van der Lee, R., Bessy, A., Chèneby, J., Kulkarni, S.R., Tan, G., et al. (2018). JASPAR 2018: update of the open-access database of transcription factor binding profiles and its web framework. Nucleic Acids Res. *46*, D260–D266. https://doi.org/10.1093/nar/gkx1126.

64. Fornes, O., Castro-Mondragon, J.A., Khan, A., van der Lee, R., Zhang, X., Richmond, P.A., Modi, B.P., Correard, S., Gheorghe, M., Baranašić, D., et al. (2020). JASPAR 2020: update of the open-access database of transcription factor binding profiles. Nucleic Acids Res. *48*, D87–D92. https://doi.org/10.1093/nar/gkz1001.

65. Wu, T., Hu, E., Xu, S., Chen, M., Guo, P., Dai, Z., Feng, T., Zhou, L., Tang, W., Zhan, L., et al. (2021). clusterProfiler 4.0: A universal enrichment tool for interpreting omics data. Innovation *2*, 100141. https://doi.org/10.1016/j.xinn.2021.100141.

66. Wickham, H. (2016). ggplot2: Elegant Graphics for Data Analysis, Second Edition (Springer Nature). https://doi.org/10.1007/978-3-319-24277-4.

STAR★METHODS

KEY RESOURCES TABLE

REAGENT or RESOURCE	SOURCE	IDENTIFIER
Antibodies		
Chicken anti-GFP	Abcam	Cat#ab13970; RRID: AB_300798v
Mouse anti-TUJ1	Merck/Sigma-Aldrich	Cat#T8660; RRID: AB_477590
Rabbit anti-PAX6	Abcam	Cat#ab195045; RRID: AB_2750924
Guinea pig anti-PAX6	Oasis Biofarm	Cat#OB-PGP078
Guinea pig anti-EOMES	Oasis Biofarm	Cat#OB-PGP022-02
Rat anti-GFAP	Thermo Fisher Scientific	Cat#13–0300; RRID: AB_2532994
Rabbit anti-GFAP	DAKO	Cat#Z0334; RRID: AB_10013382
Guinea pig anti-GFAP	Oasis Biofarm	Cat#OB-PGP055-02
Rat anti-Ctip2	Abcam	Cat#ab18465; RRID: AB_2064130
Rabbit anti-Doublecortin (DCX)	Abcam	Cat#ab18723; RRID: AB_732011
Guinea pig anti-Doublecortin (DCX)	Merck Millipore	Cat#ab2253; RRID: AB_1586992
Rabbit anti-H3K27AC	Active motif	Cat#39034; RRID: AB_2561016
Mouse anti-NeuroD1	Abcam	Cat#ab60704; RRID: AB_943491
Rabbit anti-NeuroD1	Abcam	Cat#ab205300; RRID: AB_3083561
Rabbit anti-vGluT1	Synaptic Systems	Cat#135302; RRID: AB_887877
Chicken anti-MAP2	Abcam	Cat#ab5392; RRID: AB_2138153
Rabbit anti- S100β	Abcam	Cat#ab52642; RRID: AB_882426
Mouse anti-S100β	Sigma	Cat#S2532; RRID: AB_477499
Mouse anti- Vimentin	Millipore	Cat#MAB3400; RRID: AB_94843
Rabbit anti-Olig2	Millipore	Cat#AB9610; RRID: AB_570666
Mouse anti-GAD67	Millipore	Cat#MAB5406; RRID: AB_2278725
Rabbit anti-TBR1	Abcam	Cat#ab31940; RRID: AB_2200219
Rabbit anti-NeuN	Merck	Cat#ABN78; RRID: AB_10807945
Mouse anti-FLAG	Sigma	Cat#F1804; RRID: AB_262044
Rat anti-KI67	Invitrogen	Cat#14-5698-82; RRID: AB_10854564
Rabbit anti-AQP4	Proteintech	Cat#16473-1-AP; RRID: AB_2827426
Guinea pig anti- SATB2	SYSY	Cat#327004
Donkey anti-mouse Alexa Fluor 488	Thermo Fisher Scientific	Cat#A21202; RRID: AB_141607
Donkey anti-rabbit Alexa Fluor 488	Thermo Fisher Scientific	Cat#A21206; RRID: AB_2535792
Goat anti-chicken Alexa Fluor 488	Thermo Fisher Scientific	Cat#A11039; RRID: AB_2534096
Donkey anti-rabbit Alexa Fluor 555	Thermo Fisher Scientific	Cat#A31572; RRID: AB_162543
Donkey anti-mouse Alexa Fluor 555	Thermo Fisher Scientific	Cat#A31570; RRID: AB_2536180
Goat anti-guinea pig Alexa Fluo 555	Thermo Fisher Scientific	Cat#A21435; RRID: AB_2535856
Donkey anti-rat Alexa Fluo 555	Jackson immuno research	Cat#712-165-150; RRID: AB_2340666
Donkey anti-mouse Alexa Fluor 647	Thermo Fisher Scientific	Cat#A31571; RRID: AB_162542
Goat anti-rat Alexa Fluor 647	Thermo Fisher Scientific	Cat#A21247; RRID: AB_141778
Donkey anti-rabbit Alexa Fluor 647	Thermo Fisher Scientific	Cat#A31573; RRID: AB_2536183
Donkey anti guinea pig Alexa Fluo 647	Jackson immuno research	Cat#706-605-148; RRID: AB_2340476
DAPI	Roche	Cat#70508621
Bacterial and virus strains		
pCAG::GFP	Guo et al.[16]	N/A
pCAG::NeuroD1-IRES-GFP	Guo et al.[16]	N/A

(*Continued on next page*)

Continued

REAGENT or RESOURCE	SOURCE	IDENTIFIER
pCAG::NeuroD1ERT2-IRES-GFP	This paper	N/A
lentivirus U6:XX-shRNA	This paper	N/A
Critical commercial assays		
Hyperactive Universal CUT&Tag Assay Kit for Illumina Pro	Vazyme	TD904
GEXSCOPE Single Cell RNA Library Kit	Singleron	4180012
Chromium Next GEM Single Cell ATAC Library & Gel Bead Kit v1.1	10× Genomics	PN-1000176
VAHTS Universal V8 RNA-seq Library Prep Kit	Vazyme	NR605
Deposited data		
Single-cell datasets	This paper	GSA: CRA011729
Cut&Tag datasets	This paper	GSA: CRA017418
NeuroD1_ChIP-seq dataset(1)	Pataskar et al.[22]	GEO: GSE65072
NeuroD1_ChIP-seq dataset(2)	Matsuda et al.[24]	GEO: GSE104435
NeuroD1_ChIP-seq dataset(3)	Akol et al.[25]	GEO: GSE189119
Oligonucleotides		
Primers for RT-qPCR, see Table S4	This paper	N/A
shRNA sequence for Scramble (Negative control): CCTAAGGTTAAGTCGCCCTCG	This paper	N/A
shRNA sequence for *Pax6*: GCAGACGGCATGTATGATA	This paper	N/A
shRNA sequence for *Eomes*: GGGCAATAAGATGTATGTTCA	This paper	N/A
shRNA sequence for *Hes6*: GACCTGTGTTCTGACCTAGAG	This paper	N/A
shRNA sequence for *Meis2*: GAGCCAAGGAGCAGCGTATAG	This paper	N/A
Software and algorithms		
Original code	This paper	https://github.com/lixining2020/Identification-of-the-core-regulatory-program-driving-NEUROD1-induced-neuronal-reprogramming/tree/main
CeleScope	Singleron	v1.6.0
STAR	Dobin et al.[43]	v2.6.1b
FeatureCounts	Liao et al.[44]	v2.0.1
DoubletFinder	McGinnis et al.[45]	v2.0.3
Seurat package	Hao et al.[46]	v4.0.3
ClusterProfiler	Yu et al.[47]	v3.4.0
Monocle3	Cao et al.[48]	v3.0
Monocle2	Qiu et al.[49]	V2.26.0
ARACNe-AP	Lachmann et al.[50]	v1.0.0
HdWGCNA	Samuel Morabito et al.[51]	v0.2.17
Ggalluvial	Brunson et al.[52]	V0.12.3
Cell Ranger ATAC	10× Genomics	v.2.0.0
ArchR	Granja et al.[53]	v1.0.1
MACS2	Feng et al.[54]	v2.2.7
chromVAR	Schep et al.[55]	v1.12.0
FastQC	Andrews et al.[56]	v0.11.9
RSEM	Li et al.[57]	V1.3.3
DESeq2	Love et al.[58]	V1.30.1

METHOD DETAILS

Experimental model and study participant details

Postnatal day 2–3 Sprague-Dawley rat (female or male, Guangdong Medical Laboratory Animal Center, Foshan, China) were used for primary astrocyte culture. Sprague-Dawley rat E16.5 pups (female or male, Charles River, Beijing, China) were used for primary neuron culture and single cell RNAseq. The primary cells were tested negative for mycoplasma (MycoAlert mycoplasma detection kit, Lonza, Rockland, ME) before the experiments.

Primary cell culture

Astrocytes were cultured as previously described with several modifications.[59] Briefly, the cortices from postnatal day 2–3 Sprague-Dawley rat were dissected and dissociated with 0.15% trypsin-EDTA (a mixture of 0.05% Trypsin-EDTA:0.25% Trypsin-EDTA at 1:1 volume ratio) for 15 min. The cell suspension was then seeded in non-coated flasks for expansion with the medium containing DMEM/F12 (supplemented with 4.5 g/L glucose, 2 mM L-glutamine), 10% fetal bovine serum (FBS, Australia origin) and 1% penicillin/streptomycin in a 5% CO_2 and 37°C incubator (All reagents provided by Thermo Fisher scientific, Grand Islands, NY). After 7–9 days, cell confluence reached ~90%. Non-astrocytic cells, including microglia, neurons, oligodendrocytes and their progenitors, were vigorously shaken off and the attached cells were reseeded in astrocyte maintenance medium containing DMEM/F12 (supplemented with 3.5 mM glucose, 2 mM L-glutamine), 2% B27, 10% FBS and 1% penicillin/streptomycin. The astrocyte culture was passaged 4 times to eliminate the neural stem cells before subsequent experiments.

Primary neurons were isolated from cortices of Sprague-Dawley rat E16.5 pups as described previously.[60] Briefly, the cortices were dissected in ice-cold artificial CSF (pre-bubbled with 95% O_2::5% CO_2), cut into fine pieces and incubated with 7.5 units/mL papain solution containing L-cysteine (1 mM), EDTA (0.5 mM) and DNase I (150 units/mL), dissolved in EBSS (equilibrated with 95% O2:5%CO2) at 34°C for 30 min. Then, the tissue was triturated with 200 μL pipet tips and filtered through a 70 μm cell strainer (BD, Franklin Lakes, NJ). Cell pellet was collected by centrifuged at 300 g for 5 min and then resuspended in 3 mL Ovomucoid protease inhibitor with FBS (Inhibitor-BSA Vial [LK003182], Worthington, Lakewood, NJ). To remove the debris, the cell suspension was further centrifuged at 70 × g, 6min. The cell pellets were resuspended in the medium containing DMEM/F12 (supplemented with 3.5mM glucose, 2 mM L-glutamine), 2% B27, 1% FBS and 1% penicillin/streptomycin and seeded at the density of 15,000–20,000 cells/12mm poly-D-Lysine coated coverslip. 5 days later, when the neurites appeared, 200 μg/mL L-ascorbic acid (Merck/Sigma-Aldrich), 1 μM cyclicadenosine monophosphate (Merck/Sigma-Aldrich), 1 μg/mL laminin (Merck/Sigma-Aldrich), 20 ng/mL brain-derived neurotrophic factor (Peprotech, Rocky Hill, NJ, USA), 10 ng/mL neurotrophin-3 (Peprotech), and 10 ng/mL insulin-like growth factor (Peprotech) were added and the medium was changed every 2–3 days.

All animal procedures have been approved by Jinan University Institutional Animal Care and Use Committee (Approval No. IACUC-20180330-06) and we confirm that all experiments conform to the relevant regulatory standards.

Retrovirus production

Retroviral vectors, *CAG::GFP* (GFP retrovirus), and *CAG::NeuroD1-IRES-GFP* (ND1 retrovirus) were obtained from the previous study.[16] We chose the CAG promoter that can constitutively promote GFP expression to trace the fate of ND1-transduced astrocytes for subtype characterization and electrophysiological analysis at 30 DPI. The constitutive promoter can enhance the GFP expression for tracing up to 30 days. Retroviral vector *CAG::NeuroD1ERT2-IRES-GFP* (ND1ERT2 retrovirus) was constructed by replacing NeuroD1 opening reading frame with a fusion of *NeuroD1* cDNA together with the ERT2 domain of the estrogen receptor. All viruses were packaged and concentrated as previously described.[16] The titer of viral particles was about 1 × 10^8 transfer units/mL, which was determined after transduction of HEK293T cells.

In vitro AtN conversion

Primary astrocytes at passage 5 were seeded at the density of 10,000–12,000 cells on poly-D-lysine (Merk/Sigma-Aldrich)-coated glass coverslips (12 mm in diameter, Glaswarenfabrik Karl Hecht GmbH &Co., Sondheim, Germany) in astrocyte maintenance medium. After culturing for 24 h, when the cell confluence reached 70–80%, the retrovirus was added at 5–10 MOI. Next day, the medium was switched to conversion medium containing DMEM/F12 supplemented with 3.5 mM glucose, 2 mM L-glutamine, 2% B27, 1% FBS, and 1% penicillin/streptomycin. Five days post-infection when neurite-like processes appeared, 200 μg/mL L-ascorbic acid (Merck/Sigma-Aldrich), 1 μM cyclicadenosine monophosphate (Merck/Sigma-Aldrich), 1 μg/mL laminin (Merck/Sigma-Aldrich), 20 ng/mL brain-derived neurotrophic factor (Peprotech, Rocky Hill, NJ, USA), 10 ng/mL neurotrophin-3 (Peprotech), and 10 ng/mL insulin-like growth factor (Peprotech) were added. During the conversion, half the medium was changed every other day.

To investigate the role of histone deacetylation during AtN transdifferentitaion, SGC-CBP30 (5 μM dissolved in DMSO, Selleck) was added to the conversion medium based at indicated dates.

To activate the ND1-ERT2, 4-OHT (1 μM dissolved in ethanol, Sigma) was added to the conversion medium at indicated dates.

RNA interference

Lentiviral vectors encoding *Eomes*, *Hes6* and *Mesi2* shRNA or a scramble were constructed by Packgene Biotech. Inc (Guangzhou, China). The sequences for shRNA are listed in the key resources table. To test the knock-down efficiency, cells transduced with

lentivirus *U6::Hes6/Mesi2-shRNA* or *U6:scramble* along with retrovirus ND1 were harvested 3 days after virus infection. RNA was extracted using ReliaPrep RNA Cell Miniprep System (Promega). CDNA was reverse-transcribed using PrimeScript RT reagent Kit (Takara). Real-time quantitative PCR was performed using QuantiNova SYBR Green RT-PCR Kit (Qiagen) according to the manuals on CFX Real-Time qPCR system (BioRad). Primers used in this study were also listed in the key resources table.

Immunofluorescence

Cells were fixed with 4% paraformaldehyde for 15 min and then incubated in 0.01% Triton X-100 in PBS for 10 min at room temperature. After three washes with PBS, 3% bovine serum albumin (BSA, Merck/Sigma-Aldrich) in PBS was added as blocking buffer and incubated for 1 h. Then cells were incubated with the indicated primary antibodies diluted in 1% BSA at 4°C overnight. 0.2% PBST (Tween 20 in PBS) was used to wash away the unbound antibodies. Next, 1:1000 diluted secondary antibodies were added and incubated for 1 h at room temperature. Finally, after washed by 0.2% PBST three times, 0.5 μg/mL DAPI (4′,6-diamidino-2-phenylindole, F. Hoffmann-La Roche, Natley, NJ, USA) was added to counterstain the nuclei. The coverslips were mounted on glass slides using anti-fading mounting medium (DAKO, Carpinteria, CA, USA).

Brains were collected and fixed with 4% paraformaldehyde at 4°C for 2–6 h. After fixation, the tissues were washed in cold PBS three times and transferred to 30% sucrose at 4°C until sank. The tissues were then embedded with O.C.T. (Tissue-Tek, Torrance, CA) and cryosection at 15 μm thickness. The sections were washed 3 times with PBS before subjected to antigen retravel (in 95°C citrate buffer for 10 min). Sections were incubated in blocking buffer (5% normal donkey serum, 3% BSA, and 0.2% PBST) at room temperature for 1 h and then incubated with primary antibodies for 24–48 h at 4°C. Thereafter, brain sections were rinsed with 0.2% PBST and incubated with corresponding secondary antibodies and DAPI for 2 h at room temperature, followed by an extensive wash with 0.2% PBST. Finally, the stained brain sections were mounted with mounting medium (VECTASHIELD, VECTOR Laboratories, Burlingame, CA, USA) and sealed with nail polish. Antibodies used in this study were listed in Supplemental Data 3.

Images were collected with a fluorescence microscope (Axio Imager Z2, Zeiss) for quantification and with a confocal microscope (LSM880, Zeiss) for representative image display.

Electrophysiological recording

Whole-cell recordings were performed on transdifferentiated neurons at 30 DPI or primary neurons at 30 DIV (days *in vitro*) using Multiclamp 700A patch-clamp amplifier (Molecular Devices, Palo Alto, CA) as described before,[61] and the chamber was constantly perfused with a bath solution consisting of 126 mM NaCl, 2.5 mM KCl, 1.25 mM NaH2PO4, 26 mM NaHCO3, 2 mM MgCl2, 2 mM CaCl2 and 10 mM glucose. The pH of bath solution was adjusted to 7.3 with NaOH, and osmolarity was at 310–320 mOsm/L (all reagents provided by Merck/Sigma-Aldrich). Patch pipettes were pulled from borosilicate glass (3–10 MΩ) and filled with a pipette solution consisting of 126 mM K-Gluconate, 4 mM KCl, 10 mM HEPES, 4 mM Mg2ATP, 0.3 mM Na2GTP, 10 mM PO Creatnine (pH 7.3 adjusted with KOH, 290 mOsm/L). For voltage-clamp experiments, the membrane potential was typically held at −70 or −80 mV. Data was acquired using pClamp 10 software (Molecular Devices, Palo Alto, CA), sampled at 20 kHz, and filtered at 3 kHz. Na+ and K+ currents and action potentials were analyzed using pClamp 10 Clampfit software. Spontaneous synaptic events were analyzed using MiniAnalysis software (Synaptosoft, Decator, GA). All experiments were conducted at room temperature.

Single-cell suspension acquisition

For culture cells, the attached cells at the indicated time points were dissociated using 0.05% Trypsin-EDTA to get single cell suspension. The procedure for preparing the single cell suspension from the cortices was similar to that for preparing primary neuron culture. The cell pellets were resuspended in sterile-filtered washing buffer (Dulbecco's PBS containing sodium pyruvate, streptomycin sulfate, kanamycin monosulfate, glucose and calcium chloride; Sigma-Aldrich, D4031) containing 0.5% BSA.

CUT&Tag experiments

GFP^+ cells were sorted with fluorescence-activated cell sorting (FACS) using BD FACSAria III cell sorter at the indicated time points (1, 2 and 5 DPI). For the Day 0 start cells, no cell sorting was conducted. 50,000 cells per test were pelleted and proceeded to CUT&Tag experiments following the manufacturer's instruction with a hyperactive universal CUT&Tag Assay kit for Illumina Pro (Vazyme, TD904). Two replicates were included for each test. All primary antibodies used in our CUT&Tag experiments were ChIP-grade including NeuroD1 (Cell Signaling, 4373), H3K4me3 (Millipore, 07–473), H3K9me3 (abcam, ab8898), H3K27me3 (Cell Signaling, 9733), H3K27ac (Active Motif, 39133) and normal rabbit IgG (Cell Signaling, 2729). The sequencing libraries were sequenced on Nova6000 of Illumina with PE150 reads.

scRNA-seq and scATAC-seq library preparation and sequencing

For scRNA-seq, cells were barcoded through the Singleron Matrix instrument using the GEXSCOPE Single Cell RNA Library Kit contain GEXSCOPE microchip, barcoding beads, and reagents for transcriptome amplification and library construction (Singleron Biotechnologies, 4180012). The sequencing libraries were prepared according to the manufacturer's instructions and sequenced on Nova6000 of Illumina with PE150 reads.

For scATAC-seq, nuclei were isolated according to 10× genomics protocol CG000169 (Demonstrated Protocol Nuclei Isolation ATAC Sequencing Rev E). scATAC–seq libraries were generated using the Chromium Single Cell ATAC V1 Library & Gel Bead Kit. All libraries were sequenced using MGI2000 with PE100 reads.

Bulk RNA-seq experiments

GFP^+ cells were sorted with fluorescence-activated cell sorting (FACS) using BD FACSAria III cell sorter at 3 DPI after ND1 retrovirus and shRNA lentivirus (for Scramble, *Hes6* or *Eomes*) infection. Total RNA was extracted using RNeasy Mini Kit (Qiagen, 74106). Subsequently, mRNA was captured using VAHTS mRNA Capture Beads (Vazyme #N401). RNA-seq libraries were prepared using VAHTS Universal V8 RNA-seq Library Prep Kit (Vazyme, NR605) following the manufacturer's instructions. The sequencing libraries were sequenced on SURFSeq 5000 sequencer with PE150 reads.

scRNA-seq data analysis

Raw reads were processed to generate gene expression profiles using CeleScope v1.6.0 pipeline (https://github.com/singleron-RD/CeleScope) with default parameters. Briefly, barcodes and UMIs were extracted from R1 reads and corrected. Adapter sequences and poly A tails were trimmed from R2 reads. The clean R2 reads were then aligned to the Rattus norvegicus genome (mRatBN7.2) using STAR (v2.6.1b).[43] Uniquely mapped reads were assigned to exons with FeatureCounts (v2.0.1).[44] Successfully assigned reads with the same cell barcode, UMI and gene were grouped together to generate the gene expression matrix for further analysis.

Genes detected in less than 10 cells were removed. DoubletFinder (v2.0.3)[45] was used to filter potential doublets for each sample. Cells were discarded if they met any of the following conditions: 1) expressed less than 1000 genes; 2) detected with more than 10% of mitochondrial genes; 3) contained reads number outside the range of 10^(mean(log10(reads number)) ± 2*sd(log10(reads number))).

After stringent quality control, remained cells were analyzed using Seurat package (v4.0.3).[46] The filtered count matrix was firstly log normalized using NormalizeData() function. Next, top 2000 highly variable genes were extracted by FindVariableFeatures() function, and scaled to compute principal components through ScaleData() and RunPCA(), respectively. The mutual nearest neighbors (MNN) method was used to alleviate the batch effect. Unsupervised clustering was performed on the scaled and batch corrected data by FindNeighbour() and FindCluster() function using the top 20 PCs. Uniform Manifold Approximation and Projection (UMAP) was employed to visualize the result of clustering. Cellular state labels were assigned to each cluster based on marker genes reported by FindAllMarkers() function, and we manually validated these cell state labels according to previously reported marker genes, such as *Gfap* for astrocytes and *Dcx* for newborn neuron. ClusterProfiler (v3.4.0)[47] was used to characterize each cellular states.

Trajectory analysis

A trajectory graph was constructed using Monocle3 (v3.0)[48] on UMAP coordinates from Seurat. Cells from D0 were selected as root cells. Pseudotime inference was performed using order_cells() function. We also took advantages of Monocle2[49] to describe the cellular state divergences. To compare the gene expression between two paths, we used branched expression analysis modeling (BEAM)[62] and visualized the results using the plot_genes_branched_heatmap() and plot_genes_branched_pseudotime() function.

Key transcription factor analysis

To identify the key regulators that drive the differentiation process, we first used ARACNe-AP[50] (v1.0.0) to build transcriptional regulatory networks. In brief, Rattus Norvegicus transcription factors in AnimalTFDB and gene expression matrix from Ast and Neu states, which were described by monocle2, were taken as input to the ARACNe-AP. Then, MARINa algorithms, implemented by R package ssmarina (v1.01) was used to analyze the master regulatory for each differentiation route.

WGCNA analysis

HdWGCNA (v0.2.17)[51] was used to construct co-expression networks across different cellular states. Briefly, we aggregated similar cells into several small groups by running MetacellsByGroups() function on Seurat object. Soft power threshold was inferred using TestSoftPowers() function. The co-expression network was finally constructed by running ConstrucNetwork() function. The module eigengenes (MEs) were calculated with ModuleEigengenes() function. The hub genes for each module were identified using ModuleConnectivity() and ModuleExprScore() function.

Mapping *in vitro* cells to *in vivo* references

To annotate *in vitro* query datasets based on the *in vivo* cortical reference data, we first projected the PCA structures of a reference onto the query by running FindTransferAnchors() function. Then, *in vitro* cells were classified based on *in vivo* cell type labels using TransferData() function. To guarantee an accurate annotation, we removed predicted reference cell types in which less than 50 cells in a cell cluster were assigned to. Ggalluvial[52] was used to visualize the prediction results.

scATAC-seq data analysis

scATAC-seq data processing. Raw sequencing data were converted to fastq format using 'cellranger-atac mkfastq' (10× Genomics, v.2.0.0). scATAC-seq reads were aligned to the Rattus norvegicus genome (mRatBN7.2) and quantified using 'cellranger-atac count'

(10× Genomics, v.2.0.0). Fragment data was loaded into ArchR (v1.0.1)[53] for quality control and downstream analysis. In brief, fragments on Y chromosome and mitochondrial DNA were removed. Cells with less than 1,000 or more than 100,000 fragments were filtered. We additionally identified and discarded potential doublets by using add Doublet Scores () function. To guarantee a high signal-to-noise ratio, cells with a TSS enrichment score less than 4 were also excluded in subsequent analyses.

scATAC-seq clustering and dimensionality reduction. To cluster scATAC-seq data and visualize cell embedding in a reduced dimension space, such as UMAP, we first applied iterative latent semantic indexing (LSI) on the top 25,000 accessible 500-bp tiles by running addIterativeLSI() function. Clustering was performed using addClusters() function with 'resolution' set as 0.8. An UMAP representation was obtained by running addUMAP() function with 'minDist' parameter set to 0.6.

Label transfer. To annotate scATAC-seq clusters, we first calculated gene score by running addGeneScoreMatrix() function to estimate gene expression level based on chromatin accessibility data. Then, we implemented canonical correlation analysis (CCA) by performing addGeneIntegrationMatrix() function for a preliminary unconstrained integration of scRNA-seq and scATAC-seq datasets. To further refine the integration results, we determined the most enriched scRNA-seq based cell labels in each of the scATAC-seq clusters, and then performed a second round of integration by constraining the scATAC-seq clusters to the most corresponding scRNA-seq based cell types. We validated the label transferred results by known cell type marker genes.

scATAC-seq peak identification. Since the extreme sparsity in scATAC-seq dataset, which may hinder the peak identification, we created pseudo-bulk replicates by grouping cells from the same clusters using addGroupCoverages() function. Cluster specific peaks were called using those pseudo-bulk replicates with MACS2 (v2.2.7)[54] with '-g' parameter set to 2.6 + 10e9. The peaks were visualized using plotBrowserTrack() function.

scATAC-seq motif accessibility deviations. We used chromVAR[55] to predict the enrichment of TFs for each cell type. The chromVAR deviation scores were calculated by running addDeviationsMatrix() function. The position weight matrices (PWM) used in the function were obtained from the JASPAR 2018[63] and JASPAR 2020 database.[64]

Identification of peak-to-gene links. Peaks were linked to gene based on a correlation approach, which was implemented in ArchR by running add Peak2GeneLinks() function. Briefly, peaks were associated to the TSS of genes within a 250kb genomic distance, and the Pearson correlation was calculated between scATAC-seq and scRNA-seq values. Only peak-to-gene pairs with $r > 0.35$ were retained.

CUT&Tag data processing

CUT&Tag reads were firstly quality checked using FastQC. Then, adaptor trimming, and quality filtering was carried out by TrimGlore. Bowtie2 (v 2.4.1) was used to align the paired-end clean reads to Rattus norvegicus genome with following parameter: –local –very-sensitive –no-mixed –no-discordant. Samtools (v1.15.1) was used to convert SAM file into BAM format. BAM file was then sorted and indexed. Duplicate reads in the bam file were identified and removed by Picard (v3.0.0) using MarkDuplicates function. To avoid any technical issues of CUT&Tag technique, we excluded reads which were in the IgG reads mapping region from each sample. The peaks were then called using MACS2 (v2.2.7) with the '-g' parameter set to 2.6e9 and '-q' parameter set to 0.0001. BedGraphToBigWig (v2.8) was used to convert Bedgraph (bdg) file into bigwig format, which was then visualized using Itegrative Genomics Viewer (IGV v2.9.4). Peaks were annotated using Homer (v4.11.1) by annotatePeaks.pl function. NeruoD1 motif enrichment analysis was performed by findMotifsGenome.pl function. Peak signal distribution at NeuroD1 binding sets was calculated using computeMatrix in deepTools.

Inferring ND1 target genes and ND1 network using CUT&Tag and scRNA-seq data

To obtain confident NeuroD1 target genes, we first selected genes which were bound by NeuroD1 in promoter or distal regions from NeuroD1 CUT&Tag dataset. Then, we tested whether the corresponded genes were differentially expressed in neuronal cells defined in scRNA-seq data. Genes with adjusted p-values <0.05 and $|avg\_logFC| > 0.5$ were considered as potential NeuroD1 targets. The GENIE3 (V1.27) was used to infer the NeuroD1 regulatory network. The NeuroD1 target genes present in Rattus norvegicus TF Database were set as potential regulators. The network was visualized by cytoscape.

RNA-seq data preprocessing

Raw sequencing reads underwent initial quality assessment utilizing FastQC.[56] Subsequently, the validated reads were aligned to Rattus norvegicus genome (genome-build-accession NCBI: GCF_015227675.2) employing the STAR[43] with default parameters. Gene expression levels were quantified using RSEM.[57] To assess batch effects and visualize sample distributions, principal component analysis (PCA) was conducted. Differentially expressed genes (DEGs) were identified for each comparisons using DESeq2.[58] To evaluate the function of DEGs, enrichment analyses, including KEGG pathway enrichment analysis and GO enrichment analysis, were performed using clusterProfiler.[65] The R package ggplot2 was used for data visualization.[66]

QUANTIFICATION AND STATISTICAL ANALYSIS

Immunofluorescence analysis

Quantification of immunostaining was performed by Zeiss ZEN 2.3 software (blue edition, Göttingen, Germany) using images captured at 20× objective magnification (464.9 μm × 464.9 μm) by a fluorescence microscope (Axio Imager Z2, Zeiss). Parameters

for image capturing and post-analysis were adjusted to the same values for each antigen tested. 15–20 random fields per coverslip were chosen and 3–4 coverslips were used per cell batch. Three cell batches isolated in three independent experiments were used.

Real-time qPCR analysis

The relative expression levels of the target genes were determined using the $2^{-\Delta\Delta Ct}$ method, with endogenous reference gene *Gapdh* for normalization.The data were plotted as means of 3 independent experiment (using 3 batches of cells).

All values were given as mean ± SEM and presented in the related figure legends. The data were tested for significance using unpaired t test, one-way ANOVA with Tukey's test for multiple comparisons, and two-way ANOVA followed by with Sidak's multiple comparisons test (Prism 8, GraphPad). The statistical details (including *p* values and statistical tests) were elaborated in the figures and related figure legends. *p* values over 0.05 were determined as significant difference, which were labeled in the figures.